



Contents lists available at ScienceDirect

Journal of Quantitative Spectroscopy & Radiative Transfer

journal homepage: www.elsevier.com/locate/jqsrt

Optical Modeling of Single Asian Dust and Marine Air Particles: A Comparison with Geometric Particle Shapes for Remote Sensing

Joseph M. Conny^{a,*}, Robert D. Willis^b, Diana L. Ortiz-Montalvo^a^a Materials Measurement Science Division, National Institute of Standards and Technology, Gaithersburg, MD, 20899-8372 U.S.^b Office of Research and Development, U.S. Environmental Protection Agency (retired)

ARTICLE INFO

Article history:

Received 13 January 2020

Revised 30 June 2020

Accepted 1 July 2020

Available online 3 July 2020

Keywords:

atmospheric aerosol

Asian dust

extinction

scattering

backscattering

particle shape

surface roughness

scanning electron microscopy

focused ion-beam tomography

FIB-SEM

discrete dipole approximation

ABSTRACT

We compare the optical properties of various geometric shapes with single atmospheric Asian dust and marine background air particles collected at Mauna Loa Observatory. Three-dimensional representations of the particles were acquired with focused ion-beam (FIB) tomography, which involves FIB milling of individual particles followed by imaging and elemental mapping with scanning electron microscopy. Particles were heterogeneous with mainly dolomite or calcite and a minor amount of iron; marine air particles contained gypsum but no iron. Extinction and backscatter fraction were calculated with the discrete dipole approximation method. Geometric shapes were grouped as ellipsoids (sphere, spheroid, ellipsoid), cuboids (cube, square prism, rectangular prism), and pyramids (tetrahedron, triangular pyramid). Each group represented a progression of shapes with 1, 2, or 3 non-identical axes. Most shapes underestimated particle extinction and overestimated the backscatter fraction. Not surprisingly, extinction and the backscatter fraction of the sphere and cube were furthest from those of the particles. While the 3-axis ellipsoid and rectangular prism were closer dimensionally to the particles, extinction and the backscatter fraction for the 2-axis spheroid and square prism, respectively, were often closer to the particles. The extinction and backscatter fraction for the tetrahedron and triangular pyramid were closer on average to the actual particles than were the other shapes. Tetrahedra have the advantage that parameterization of an aerosol model for remote sensing would not require an aspect ratio distribution. Particle surface roughness invariably decreased the backscatter fraction. While surface roughness typically contributes a minor part to overall scattering, in some cases the larger surface area of the tetrahedron and triangular pyramid sufficiently accounted for enhanced forward scattering of particles from surface roughness.

Published by Elsevier Ltd.

1. Introduction

Dust aerosols affect climate by shifting Earth's radiative balance either by direct interaction with solar and longwave radiation or indirectly by serving as cloud condensation nuclei and affecting physical processes in clouds. The largest radiative-forcing uncertainties are associated with aerosol-cloud interactions [1]. Uncertainties in the direct radiative forcing by mineral dusts are associated with the large geographic and temporal variability in the size, shape, and composition of dust particles [2]. Atmospheric dust is often assumed to be of mineral origin, i.e., natural, from large dust releasing regions such as the deserts of the Sahara, Gobi, and Taklamakan [3–5]. However, dust from agricultural land use and urban areas with uniquely anthropogenic compositions such as vehicular brake wear, wear from roads and other structures, demolition dust,

etc., contributes significantly to global dust load [6,7]. A common characteristic of mineral and urban dusts is particle shape irregularity [8–11].

Remote sensing of aerosols is typically accomplished with satellite-based spectroradiometers that detect light reflected from Earth's surface and scattered by the atmosphere, with ground-based sun photometers pointed skyward to detect sunlight scattered by aerosols, and with Lidar that detects reflected laser light that has interacted with aerosols. Examples of satellite-based instruments are VIIRS (Visible Infrared Imaging Radiometric Suite) on board the Suomi National Polar-Orbiting Partnership satellite in collaboration with the National Oceanic and Atmospheric Administration [12,13], MODIS (MODerate-resolution Imaging Spectroradiometer) on board the National Aeronautics and Space Administration's (NASA) Aqua and Terra satellites [14,15], and MISR (Multi-angle Imaging SpectroRadiometer) on board NASA's Terra satellite [16,17]. The AERONET (AErosol ROBotics NETwork) system of sun photometers provides ground-based reference data for validating

* Corresponding author.

E-mail address: joseph.conny@nist.gov (J.M. Conny).

satellite retrievals [18,19]. The CALIOP (Cloud-Aerosol Lidar with Orthogonal Polarization) infrared Lidar imager on board CALIPSO (Cloud-Aerosol Lidar and Infrared Pathfinder Satellite Observation) is used to study the indirect aerosol effect [20,21].

The most important aerosol property from remote sensing is aerosol optical depth (AOD), which is proportional to the total aerosol concentration in the air column. AOD is also the integrated extinction coefficient for the population of particles in the air column. To determine AOD from spectroradiometry an inverse modeling scheme is required. A necessary component of inverse modeling is an aerosol model. The aerosol model parameterizes the population of particles in the air column by assuming an average composition (complex refractive index) or series of compositions, one or more particle size distributions, and representative particle shape geometries. By parameterizing the particle population, the aerosol model provides input for calculating the scattering phase function (angular intensity of scattered light) and the single scattering albedo (scattering cross section divided by the extinction cross section for a single scattering event), which are then used to determine AOD [22].

A critical part of the aerosol model is representation of the shapes of real particles. Kahnert et al. [23] provide a thorough review of particle shape and its importance in remote sensing. While the optical properties of particles as spheres are easier to calculate using Lorenz-Mie theory, biaxial spheroids have long been used to account for shape irregularity in mineral dust particles [24–27]. To this end, it is well known that the phase function for spheroids differs significantly from that of spheres [28] when the imaginary part of the complex refractive index is not too large, e.g., < 0.5 [29]. Spheroids tend to correct for anomalously low scattering at side angles and high backscattering as exhibited in the phase function for spheres [10,28]. Current aerosol models for deriving AOD from MODIS and AERONET spectra use spheres for particles $< 1 \mu\text{m}$ in diameter and spheroids with size and aspect ratio distributions for particles $> 1 \mu\text{m}$ [26,30]. Mineral dust is typically in the coarse size range, e.g., $> 1 \mu\text{m}$.

Optical properties of other simplified shapes such as finite cylinders [31] and various polyhedra [10,27] have been used to model scattering by mineral dust. Models of irregularly-shaped agglomerates have been compared with spheroids in their agreement with measured optical properties of feldspar particles [32]. To account for surface roughness, surface features are often added to simple shapes. Surface roughness has been modeled with 2- and 3-D Chebyshev functions [33,34], Gaussian perturbation at the surface of spheres [35] and Gaussian random spheres [36], and particles dusted with small surface grains [37]. Stereogrammetric renderings of real particles from electron microscopy with added randomized surface features have also been used to model surface roughness [38].

It is tempting to provide more complexity to shape models to better mimic the angularity of real particles. A benefit of complex shape models is that the disorder in their morphologies allows for scattering responses to converge, suggesting that a specific shape has little effect on the retrieval of aerosol properties with remote sensing [39],[40]. Kalashnikova and Sokolik [41] generated complex shapes consisting of randomly-formed aggregates of sharp-edged rectangles and cubes along with aggregates of spheres and calculated their optical properties with compositions and sizes resembling Saharan and Asian dust. A comparison of the optical properties of these complex shapes with spheres and spheroids confirmed the need to consider shape angularity when understanding the optical behavior of mineral dust.

As particle shape in aerosol models becomes more complex, models run the risk of becoming impractical for use in remote sensing. First, retrieval of aerosol properties becomes computationally more burdensome if aerosol models require additional param-

eterization due to shape complexity. Second and perhaps more important, the more complex a particle shape becomes to where it nearly replicates real particles exactly, the less universal the shape becomes for determining aerosol properties at the mesoscale, i.e., in different regions and points in time. The argument against making shape constructs too complex for remote sensing is poignantly made by Kahnert et al. [23]. Rather than having complex particle shapes incorporated in aerosol models for remote sensing, they are perhaps more useful as reference models with which to evaluate more simplified shape models.

Determining which particle shape distribution works best in remote sensing has invariably been based on the average optical behavior of particle ensembles rather than single particles. However, the optical behavior of a shape selected for remote sensing of a particle population may not match well the behavior of an individual particle. For spheroids, distributions for size and aspect ratio may be adjusted to resemble the phase function and polarization of an ensemble of real particles. However, the refractive indices for the shapes may then not agree with the refractive indices of the actual particles. If refractive indices are made to agree, the aspect ratio distribution may not. A “universal” ensemble of spheroids to match the phase function of a population of real dust particles has been elusive [42]. Kahnert et al. [23] has warned “... one should not think that when using spheroids to mimic scattering by more complex particles, best results would be achieved using aspect ratios of the target particles for the spheroids.”

The purpose of the current work is to determine how well the optical properties of simple geometric shapes compare with the properties of single heterogeneous atmospheric dust particles. A series of shapes was employed that had the same volume, aspect ratio, and refractive indices as the actual particles. We primarily focus on the extinction efficiency and the backscatter fraction. We show the backscatter fraction in this work rather than the asymmetry parameter because the former provides a more direct indication of the extent of scattering backward from the light source.

Three groups of three-dimensional particle shapes were studied:

- Ellipsoid group: sphere, spheroid (prolate and oblate), ellipsoid
- Cuboid group: cube, square prism, rectangular prism
- Pyramid group: tetrahedron, triangular pyramid

Each group represents a progression of lower-order to higher-order shapes with lower-order shapes such as a sphere and cube having identically-sized axes in 3-D space and higher-order shapes having axes with different sizes in 3-D space. Lower-order and higher-order shapes can also be defined by the axes aspect ratio (or the height-to-width ratio). For example, square prisms and spheroids have two non-identical axes and one aspect ratio, while ellipsoids have three non-identical axes and two aspect ratios. Spheres and cubes have no aspect ratio. In the pyramid group, the tetrahedron can be defined as having identically sized axes from the center of the tetrahedron to its four vertices, and no aspect ratio. The height of the triangular pyramid is greater than that of the tetrahedron and, thus, has two axes (height and edge length) and one aspect ratio.

The shape groups can also be characterized by angularity. We define angularity as how abruptly a plane touching the surface of a shape would shift direction as it moves over the surface. The cube, square prism, and rectangular prism have high angularity because a plane moving over the surface shifts abruptly by 90° at the shapes' edge. The tetrahedron and triangular pyramid also have high angularity. In the tetrahedron, a plane moving between faces shifts abruptly by 70.5° , the face-edge-face (or dihedral) angle. The sphere, spheroid, and ellipsoid have low angularity because of their curvature. Angularity is correlated with surface area. Shapes with high angularity in this study have larger surface area.

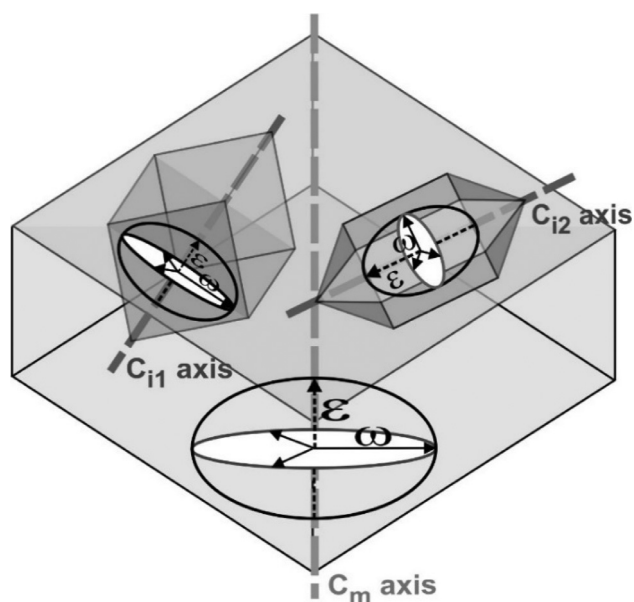


Fig. 1. Schematic from [44] of a heterogeneous particle containing two inclusion phases (dark gray) within a matrix phase (light gray). Each phase is shown with a uniaxial indicatrix which indicates the relative magnitudes of the two refractive indices, ω and ε , if vibration of the incident light were to align with the respective optical axes (C_{i1} , C_{i2} , C_m).

The particles in this work were Asian dust and background marine air particles collected at Mauna Loa Observatory (MLO) in Hawaii, U.S. In a previous paper [44], we reported on the selection of samples from MLO based on meteorological back trajectories and global aerosol maps. We also showed how particle composition was determined from scanning electron microscopy and energy dispersive x-ray spectrometry (SEM-EDX). Exact spatial representations for 13 of the particles were then created with focused ion-beam (FIB) tomography. We also reported previously the extinction efficiency and the backscatter fraction for each selected particle, calculated from the spatial representations with the discrete dipole approximation (DDA) method [45].

As we reported previously [44], two groups of Asian dust particles were studied. One group largely contained the mineral-phase dolomite ($\text{CaMg}(\text{CO}_3)_2$), the other group calcite (CaCO_3). Others have used SEM-EDX and DDA to model the optical properties of flake-like calcite particles to compare with spheroidal models [46]. DDA models of rhomboidal and flake-like calcite particles have been compared with calcite scattering measurements [47]. The Asian dust particles in our study were heterogeneous, with additional phases such as clay or feldspar minerals. In addition, the Asian dust particles contained iron. Iron oxides such as magnetite or hematite can strongly affect particle optical properties because they absorb in the visible spectrum unlike most other common minerals [48–49]. The background marine air particles were also heterogeneous but largely contained gypsum ($\text{Ca}(\text{SO}_4) \cdot 2(\text{H}_2\text{O})$) and little or no iron [44]. Mineral mass percent compositions of the 13 particles are shown in Table S1 in *Supplementary Material*.

In this work, we used a novel approach to assess the optical behavior of compositionally heterogeneous particles, as we reported previously [44]. When inclusions are embedded in a larger matrix, different spatial orientations of the inclusions will result in different refractive indices for the overall particle. If the exact positions of the inclusions within a particle are unknown, as was the case in this study, then a range of refractive indices is possible for the particle. Fig. 1 depicts how two inclusions with uniaxial optical anisotropy might be oriented in a larger phase also with uniaxial anisotropy. A uniaxial indicatrix is associated with each phase,

indicating that each phase has two refractive indices: ω (ordinary) and ε (extraordinary). The orthogonal axes of each indicatrix indicate the magnitudes of the refractive indices if vibration of the incident light wave were to align with the optical axis of each phase (C_i , for the inclusions and C_m for the matrix). We calculated an upper and lower limit to the particle's overall refractive index to reflect the range of possible refractive indices. These refractive indices were then used with the DDA method to determine the range and midpoint of possible values for the extinction efficiency and backscatter fraction for the particles calculated previously [44] and the geometric shapes in this study.

A similar comparison of the optical properties of three-dimensional shapes and single particles was reported by Lindqvist et al. [43]. Particle shape was generated from pairs of SEM images, whereby each image in the pair was collected at a slightly different angle position of the instrument stage. Corresponding points in the image pair were registered and processed mathematically to form a 3-D representation of the particle surface, a technique known as stereogrammatic shape retrieval. As in our study, particle composition was determined by EDX, and refractive indices were selected from literature. Optical properties for the 3-D representations were calculated by the DDA method for incident light in the visible (550 nm). Four dust particles were studied by Lindqvist et al.: 1) a calcite particle with magnesium and clay minerals, 2) a dolomite particle containing clay minerals, 3) a silicate particle rich in magnesium, and 4) an aggregate of likely feldspar, illite, quartz, and a clay mineral. Particle shapes included the sphere, spheroid, and a Gaussian random sphere.

While similarities exist between our work and Lindqvist et al. such as particle composition from EDX and optical properties from DDA, our work differs from Lindqvist et al. in several ways. First, we expand the number of geometric shapes to include cuboidal and pyramid shapes. Second, we employ FIB tomography to construct 3-D spatial representations rather than stereogrammatic shape retrieval. Third, we employ upper and lower limits for the refractive index of each particle to account for the variation in the spatial arrangement of inclusions within each particle. Fourth, as described in the Results section, we model the iron component of each particle as light-absorbing oxides and non-absorbing carbonates. Finally, we investigate how well geometric shape may account for particle surface roughness by smoothing the 3-D spatial representations of the particles from FIB tomography.

2. Methods

2.1. Mineral dust particles

Thirteen particles were studied: nine of Asian dust and four from background marine air. Four of the Asian dust particles contained dolomite and five contained calcite. Details were presented previously [44] on how Asian dust and background marine air aerosol at MLO were sampled, particle populations for each sample were analyzed and classified by SEM-EDX, individual particles were selected and analyzed by SEM-EDX, and how FIB tomography was performed. Briefly, 12 filter samples of particles $\leq 10 \mu\text{m}$ in size were collected over 72 hours at MLO during March and April 2011. Six samples were collected during daytime (“D” samples) and integrated over 72 hours; six nighttime (“N”) samples were collected by also integrating over 72 hours. Dust monitoring information and meteorological back trajectories were used to identify when Asian dust likely reached MLO. Automated SEM-EDX particle analysis was used to identify two classes of Asian dust particles: CaMg which was considered to contain dolomite and Ca-rich which was considered to contain calcite. In addition, one class of background marine air particles Ca-S was identified as containing gypsum. The three particle classes were distinctly different from classes of local dusts.

Table 1
Minimum and Maximum Values for Average Complex Refractive Indices¹.

| | Particle | Iron-Containing Phase | Minimum Refractive Index | | Maximum Refractive Index | |
|---------|-----------|-----------------------|--------------------------|-----------|--------------------------|-----------|
| | | | Real | Imaginary | Real | Imaginary |
| CaMg | 1D | Magnetite | 1.504 | 1.53E-03 | 1.671 | 1.73E-03 |
| | | Hematite | 1.505 | 1.69E-04 | 1.673 | 1.73E-04 |
| | | Ankerite | 1.502 | 4.68E-06 | 1.670 | 4.73E-06 |
| | 2N | Magnetite | 1.507 | 3.20E-03 | 1.652 | 3.57E-03 |
| | | Hematite | 1.509 | 3.51E-04 | 1.656 | 3.52E-04 |
| | | Ankerite | 1.503 | 8.33E-06 | 1.650 | 8.41E-06 |
| | 3D | Magnetite | 1.505 | 2.37E-03 | 1.662 | 2.67E-03 |
| | | Hematite | 1.507 | 2.60E-04 | 1.665 | 2.63E-04 |
| | | Ankerite | 1.502 | 6.01E-06 | 1.660 | 6.07E-06 |
| | 4N1 | Magnetite | 1.510 | 5.08E-03 | 1.653 | 5.67E-03 |
| | | Hematite | 1.513 | 5.47E-04 | 1.658 | 5.56E-04 |
| | | Ankerite | 1.503 | 1.18E-05 | 1.649 | 1.19E-05 |
| Ca-rich | 1D | Magnetite | 1.504 | 5.53E-03 | 1.642 | 6.15E-03 |
| | | Hematite | 1.507 | 5.94E-04 | 1.647 | 6.02E-04 |
| | | Siderite | 1.498 | 1.16E-05 | 1.640 | 1.16E-05 |
| | 2N | Magnetite | 1.520 | 4.03E-03 | 1.569 | 4.20E-03 |
| | | Hematite | 1.522 | 4.42E-04 | 1.573 | 4.01E-04 |
| | | Siderite | 1.515 | 6.80E-06 | 1.567 | 6.76E-06 |
| | 3D | Magnetite | 1.532 | 2.14E-02 | 1.660 | 2.36E-02 |
| | | Hematite | 1.544 | 2.32E-03 | 1.681 | 2.28E-03 |
| | | Siderite | 1.508 | 1.34E-05 | 1.648 | 1.34E-05 |
| | 4N1 | Magnetite | 1.503 | 3.57E-03 | 1.632 | 3.94E-03 |
| | | Hematite | 1.505 | 3.96E-04 | 1.636 | 3.91E-04 |
| | | Siderite | 1.499 | 6.89E-06 | 1.630 | 6.85E-06 |
| 4N2 | Magnetite | 1.503 | 1.83E-03 | 1.640 | 2.03E-03 | |
| | Hematite | 1.505 | 2.01E-04 | 1.642 | 2.00E-04 | |
| | Siderite | 1.501 | 5.63E-06 | 1.640 | 5.59E-06 | |
| Ca-S | 1D | Hematite | 1.523 | 1.62E-04 | 1.542 | 1.43E-04 |
| | 2N | Hematite | 1.524 | 2.27E-04 | 1.542 | 2.00E-04 |
| | 3D | (²) | 1.521 | 5.71E-06 | 1.536 | 5.715E-06 |
| | 4N | (²) | 1.521 | 2.33E-06 | 1.538 | 2.32E-06 |

¹ Determined by sequentially combining phases with the Maxwell Garnett dielectric function, Eq. (2). ² No iron was detected.

Individual particles from two daytime samples (1D, 3D) and two nighttime samples (2N, 4N) were then selected for modeling.

FIB tomography involves the sequential milling of a single particle with a gallium ion beam followed by imaging of each milled slice with SEM and element mapping with EDX [50,51]. When the ion-beam column is a component of the SEM instrument, the technique is FIB-SEM. The instrument used here was an FEI Nova NanoLab 600 Dual Beam (Thermo-Fisher Scientific, Waltham, MA, U.S.).¹ Element mapping is used to determine the composition heterogeneity of the particle. Element mapping with FIB-SEM can often identify the locations of the inclusion phases within a particle [52]. However, for the particles collected at MLO, element mapping could only identify the presence of a mineral phase in the particle for the most part, not its location within the particle.

In this work, we used DDSCAT ver. 7.3 [53] to implement the DDA method. With DDA, the particle consists of a set of dipoles that are subject to the incident electric field as well as the electric fields from neighboring dipoles. First, secondary electron images from FIB tomography were used to construct a 3-dimensional spatial model of each particle using segmentation techniques in Avizo ver. 7 (Thermo-Fisher Scientific, Waltham, MA, U.S.). Coordinates of the voxels from the 3-D spatial model were then input to DDSCAT along with complex refractive indices.

Details of how DDSCAT runs were parameterized were reported previously [44]. Briefly, the particle is defined in DDSCAT as a target in a computational lab frame. The incident light was in the visible at 589 nm. The target was rotated relative to the light source

to simulate random orientations of a particle. Two angles, Θ and Φ , specify the position of the target relative to the direction of incident light. A third angle, β , specifies the increment of rotation about the target's axis. Φ was incremented from 0° to 360° in steps of 60°. Θ was incremented 0° to 60°, 90°, 120°, and 180°, which is at uniform intervals of $\cos(\Theta)$ from 1 to -1. β was incremented from 0° to 360° in steps of 60°. The number of orientations of the target about the lab frame was 180.

2.2. Geometric shape models

For the geometric shapes, we used the "hardwired" targets in DDSCAT for the sphere, spheroid, ellipsoid, cube, square prism, rectangular prism, and tetrahedron. DDSCAT targets and shape parameters are in Table S2 in *Supplementary Material*. For the triangular pyramid, cartesian coordinates for the DDSCAT dipole positions were generated as a text file with a MATLAB script (see *Supplementary Material*). The triangular pyramid was generated with an upper and lower aspect ratio (triangular pyramid low, triangular pyramid high) to bracket the aspect ratio of the particle as close as possible.

Aspect ratios for the particles were determined from a particle's 3-D representation in Avizo. For the major axis, we determined the longest distance by inspecting all 2-D planes through the particle in the xy, xz, and yz projections. First, we select the two longest distances in the xy, xz, and yz planes, for example, the x distance in the xy and xz planes. The midpoint was then taken as the major axis.

For the aspect ratio's minor axis, we determine the orthogonal axes in the y and z directions. We measured the orthogonal y distance in the same xy plane as for the major axis. Next, we measured the shorter orthogonal axis in the y direction in a corre-

¹ Commercial products identified here specify the means by which experiments were conducted. Such identification is neither intended to imply recommendation or endorsement by the National Institute of Standards and Technology nor imply that the identified products are necessarily the best available for the purpose.

sponding yz plane. We then took the midpoint of the two y measurements as the orthogonal axis in the y direction. For the orthogonal axis in the z direction, we measured the distance in the z direction from the same yz plane used for the orthogonal axis in the y direction. Next, we measured the shorter orthogonal axis in the z direction from the xz plane. We then took the midpoint of the two z measurements as the orthogonal axis in the z direction. For the minor axis, we took the midpoint of the orthogonal axes in the y and z directions.

A similar approach was used to determine the axes for the shapes. For example, the major axis in a prolate spheroid was the major axis from the corresponding particle's major axis in the x direction. The shorter orthogonal axis in the y or z direction from the particle was taken as the minor axis for the prolate spheroid. For the ellipsoid, the major axis was similarly taken from the particle's major axis in the x direction. The two minor axes for the ellipsoid were taken from the particle's orthogonal axes in the y and z directions.

For the selected particles, we also determined sphericity [54]

$$\Psi = \frac{\pi^{1/3}(6V)^{2/3}}{A}, \quad (1)$$

where A and V are the surface area and volume of the particle, respectively, as the number of voxels on the surface and in the interior of the particle from Avizo. The sphericity of a sphere is 1.

2.3. Average complex refractive index

Complex refractive indices for the minerals were taken from the literature. Sources are reported in Tables S5 to S7 of *Supporting Information* in Conny et al. [44]. The upper and lower limits to the complex refractive index for each particle were determined as an average of the particle's mineral phases using the Maxwell Garnett dielectric function [55]. As an effective medium approximation, the Maxwell Garnett dielectric function assumes that an inclusion phase is small compared to the matrix. We apply a version of the Maxwell Garnett function that makes the approximation that inclusions are spherical [56]:

$$\epsilon_{av} = \epsilon_m \left[1 + \frac{3f \left(\frac{\epsilon_{in} - \epsilon_m}{\epsilon_{in} + 2\epsilon_m} \right)}{1 - f \left(\frac{\epsilon_{in} - \epsilon_m}{\epsilon_{in} + 2\epsilon_m} \right)} \right]. \quad (2)$$

Here, ϵ_{av} is the average dielectric function for the combined phase, f is the volume fraction of the inclusion, ϵ_{in} is the dielectric function for the inclusion phase and ϵ_m is the dielectric function for the matrix. The dielectric function is a complex number consisting of the real part $\epsilon'_{av,in,m}$ and the imaginary part $\epsilon''_{av,in,m}$. The complex dielectric function is then used to determine the complex refractive index $m_{av} = n_{av} + ik_{av}$. The real part (n_{av}) of the average refractive indices for the particle (lower and upper limits) is $n_{av} = \text{sqrt}\{[(\epsilon_{av}^{\prime 2} + \epsilon_{av}^{\prime\prime 2})^{1/2} + \epsilon_{av}^{\prime}]/2\}$. The imaginary part is $k_{av} = \text{sqrt}\{[(\epsilon_{av}^{\prime 2} + \epsilon_{av}^{\prime\prime 2})^{1/2} - \epsilon_{av}^{\prime}]/2\}$.

As shown previously [44], the average refractive indices are determined from the Maxwell Garnett dielectric constant by adding the different inclusion phases sequentially by size. First, the inclusion phase with the largest volume is added to the matrix to calculate the first average dielectric constant. This first average constant now becomes the dielectric constant for the matrix. Next, the second largest inclusion phase is added to the updated matrix to calculate the second average dielectric constant. This second average constant now becomes the dielectric constant for the matrix. The sequence continues until all inclusion phases, minus the smallest phase, are added to the matrix. The overall average dielectric constant for the particle is then calculated from dielectric constants for the cumulative matrix and the last inclusion phase. Table 1 shows the upper and lower limits to the average complex

refractive index for the particles with different forms of the minor iron phase as described below.

A drawback to using the Maxwell Garnett approximation here is that inclusions are not necessarily spherical. An additional concern regarding the sequential application of Maxwell Garnett is that the matrix may be weighted too heavily. However, in the end the matrix does not retain the dielectric constant of the initial largest phase. Rather, the matrix acquires the cumulative character of the largest phase, plus the next largest phase, and so forth to include the next to the last phase. Less satisfactory would be to apply the Maxwell Garnett approximation by defining the largest phase as the matrix, summing the volumes of the remaining phases as the inclusion phase, and calculating a weighted average dielectric constant for the inclusion phase. A case in point is particle CaMg 4N1 shown in Table 4. Here, the largest phase, dolomite, is $\leq 41\%$ of the total volume. With dolomite as the matrix, the sum of volumes for the remaining phases in this case would necessarily exceed the volume of the matrix.

2.4. Optical property modeling

Determinations of the single-scattering extinction efficiency and backscatter fraction are derived from elements of the amplitude scattering matrix and the Mueller matrix [56]. Elements of the amplitude scattering matrix (S_1 , S_2 , S_3 , and S_4) are used to determine the amplitudes of the polarity-resolved electric fields for scattered light from the incident electric fields.

More versatile in determining scattering properties is the scattering matrix equation, which consists of the 4×4 Mueller matrix and four Stokes parameters I , Q , U , V :

$$\begin{pmatrix} I_s \\ Q_s \\ U_s \\ V_s \end{pmatrix} = 1/k^2 r^2 \begin{pmatrix} S_{11} & S_{12} & S_{13} & S_{14} \\ S_{21} & S_{22} & S_{23} & S_{24} \\ S_{31} & S_{32} & S_{33} & S_{34} \\ S_{41} & S_{42} & S_{43} & S_{44} \end{pmatrix} \begin{pmatrix} I_i \\ Q_i \\ U_i \\ V_i \end{pmatrix}. \quad (3)$$

Here, $k = 2\pi/\lambda$, where λ is the wavelength of light, which was $0.589 \mu\text{m}$ in this study, and r is the distance of the scattered light to a hypothetical detector. The Mueller matrix elements are themselves combinations of amplitude scattering matrix elements S_1 , S_2 , S_3 , and S_4 [56].

For the Stokes parameters, I_s is the scattered irradiance and I_i is the incident irradiance for incident unpolarized light. Q_s is the difference between scattered irradiances for the parallel and perpendicular polarization states; Q_i is the difference in incident irradiances for the two polarization states. U_s is the difference between scattered irradiances for light that is shifted $+45$ deg. and -45 deg. from the parallel polarization state (hence, states still orthonormal as with parallel and perpendicular polarization). U_i is the difference between incident irradiances for light that is shifted as for U_s . V_s is the difference between scattered irradiances that are circularly-polarized toward left and circularly-polarized toward right. V_i is the difference between incident irradiances for light that is circularly polarized as for V_s .

The matrix element S_{11} is proportional to the ratio of scattered to incident irradiances and, thus, is proportional to scattering intensity. The degree of linear polarization by the scatterer is $-S_{12}/S_{11}$. For unpolarized incident light, the differential cross section of scattered light ($\frac{d(C_{sca})}{d\Omega}$) is proportional to the scattering intensity at a solid angle Ω :

$$\frac{d(C_{sca})}{d\Omega} = \frac{I_s}{I_i} r^2 = \frac{1}{k^2} S_{11}. \quad (4)$$

The phase function (p) is related to the differential scattering cross section, and therefore, S_{11} as follows:

$$p = \frac{1}{C_{sca}} \frac{d(C_{sca})}{d\Omega} = \frac{S_{11}}{C_{sca} k^2}. \quad (5)$$

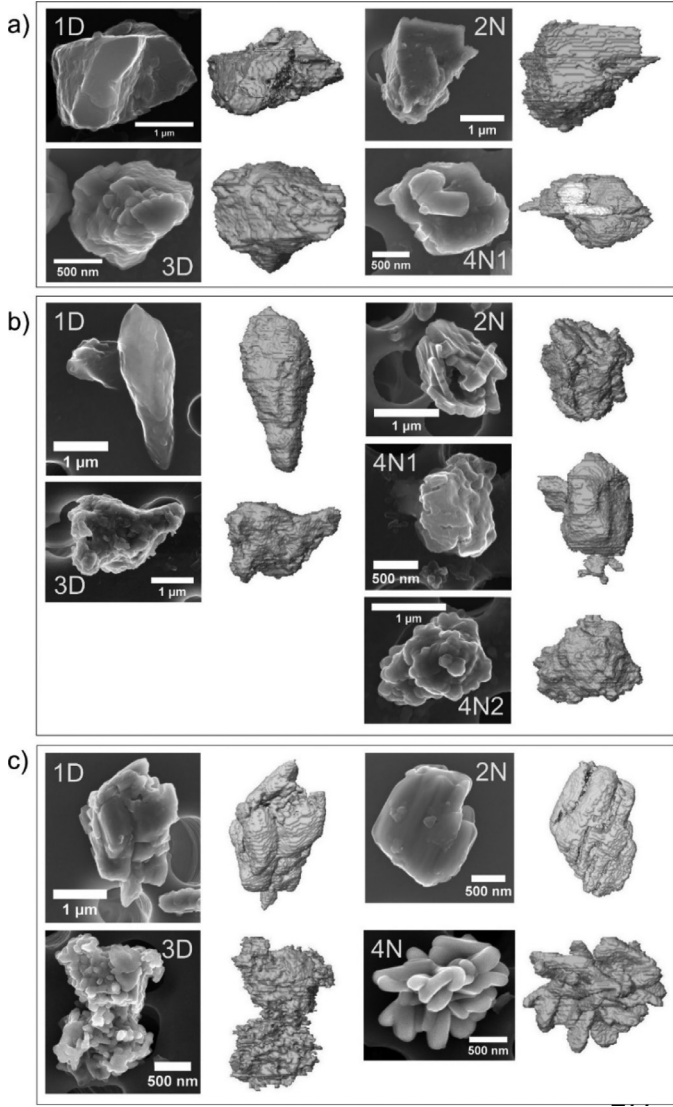


Fig. 2. Secondary electron images from SEM and 3-D representations from FIB tomography of 13 particles from the Asian dust and background marine air samples. a) and b) CaMg and Ca-rich Asian dust particles; c) Ca-S background marine air particles.

C_{sca} is the total scattering cross section. It is not a simple integration of Eq. (4), but rather involves elements of the amplitude scattering matrix [56]:

$$C_{sca} = \int_{4\pi} \frac{|\mathbf{X}|^2}{k^2} d\Omega, \quad (6)$$

$$\mathbf{X} = (S_2 \cos\Phi + S_3 \sin\Phi) \hat{\mathbf{e}}_{\parallel s} + (S_4 \cos\Phi + S_1 \sin\Phi) \hat{\mathbf{e}}_{\perp s}. \quad (7)$$

Here, $\hat{\mathbf{e}}_{\parallel s}$ is a unit vector parallel to the scattering plane, which is defined by the light source, particle, and the detector. Φ is the angle of the scattering plane in the coordinate system about the particle. $\hat{\mathbf{e}}_{\perp s}$ is the vector orthogonal to the scattering plane.

The extinction cross section C_{ext} is the sum of the absorption cross section, C_{abs} , and C_{sca} . The extinction efficiency, Q_{ext} is the extinction cross section divided by the cross-sectional area of a volume-equivalent sphere.

The backscatter fraction (BSF) is here determined as the fraction of light intensity scattered between 90° and 180° rather than directly backward at 180° . The fraction is the ratio of integrals based

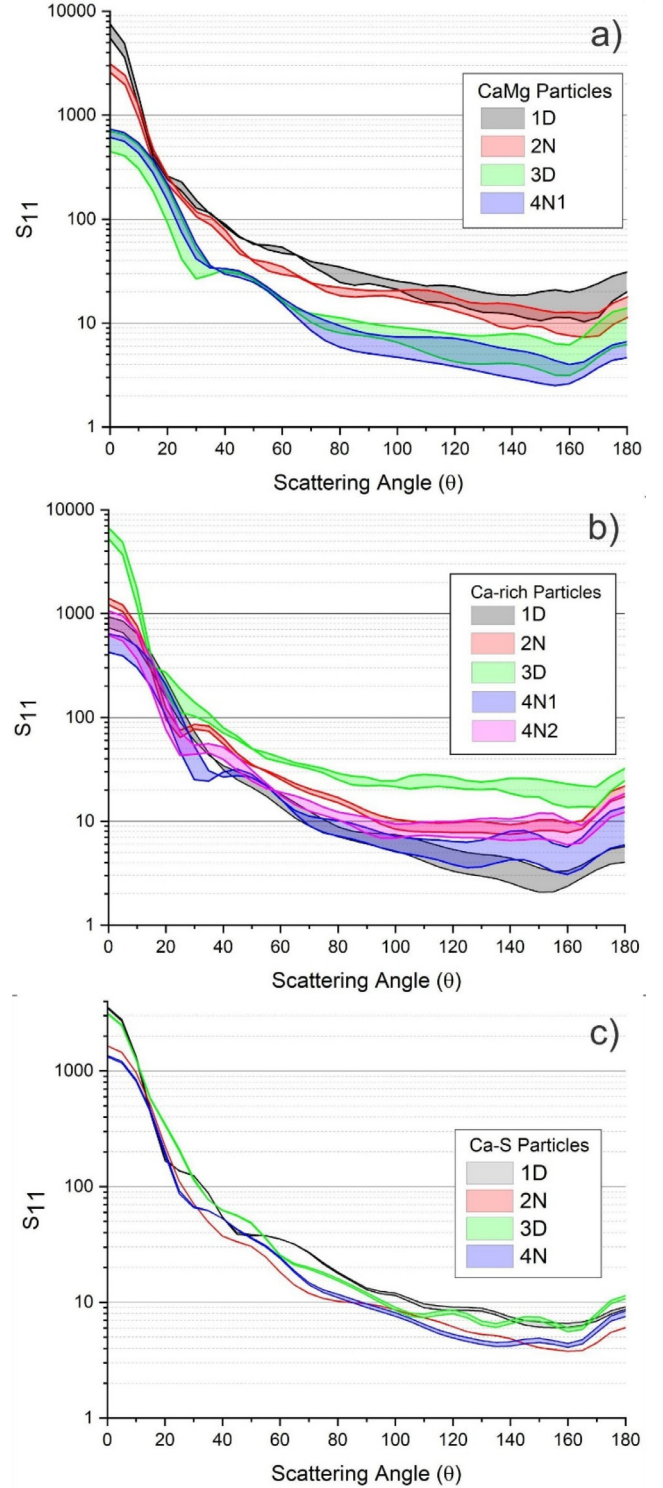


Fig. 3. S_{11} from scattering matrix versus scattering angle for Asian dust (a and b) containing hematite as the iron phase and background marine air particles (c). Ca-S particles 1D and 2N also contained iron as hematite.

on Eq. (4):

$$BSF = \int_{90}^{180} S_{11} d\Omega / \int_0^{180} S_{11} d\Omega = \sum_{90}^{180} S_{11} \Delta\Omega / \sum_0^{180} S_{11} \Delta\Omega. \quad (8)$$

Omega is determined from Eqs. 56 to 58 in Draine and Flatau, 2013 [53]:

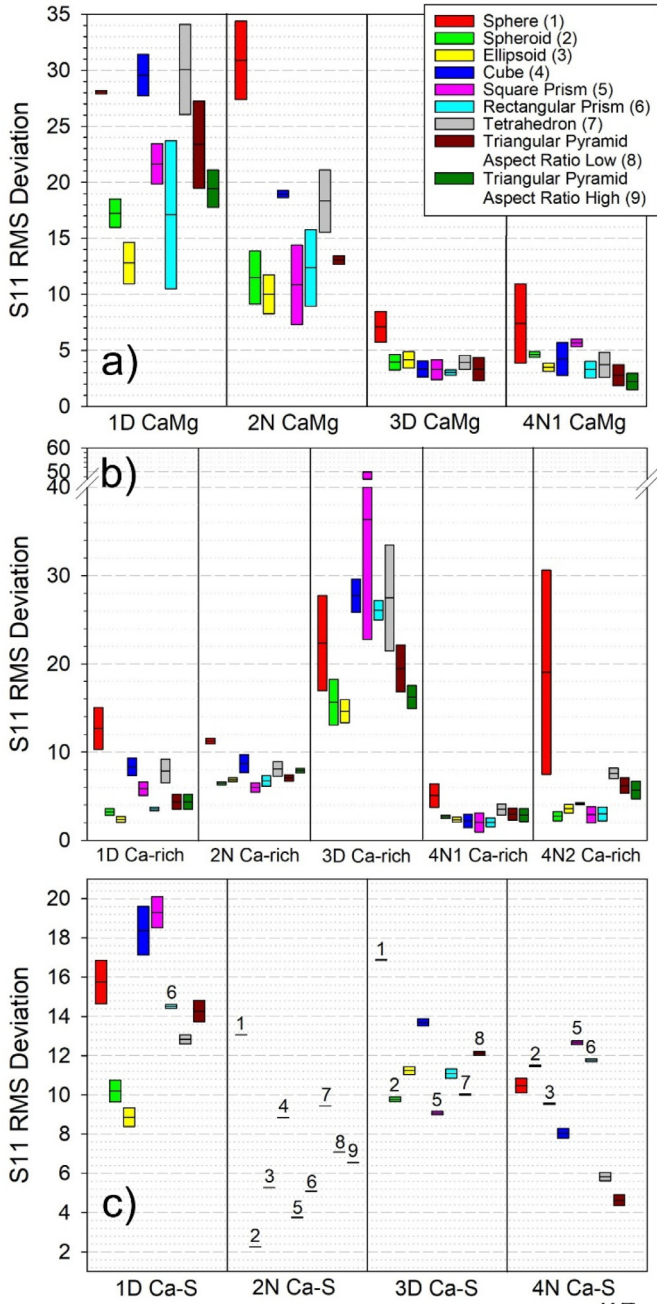


Fig. 4. Root-mean-square (RMS) deviation in S_{11} for geometric shapes from the respective particles containing hematite. a) and b) Asian dust particles; c) background marine air particles.

$$\Omega_{j,k} = \frac{\pi}{N_\phi(j)} [\cos(\theta_{j-1}) - \cos(\theta_{j+1})], \quad j = 2, \dots, N_\theta - 1, \quad (9)$$

$$\Omega_{1,k} = \frac{2\pi}{N_\phi(1)} \left[1 - \frac{\cos(\theta_1) + \cos(\theta_2)}{2} \right], \quad (10)$$

$$\Omega_{N_\phi,k} = \frac{2\pi}{N_\phi(N_\theta)} \left[\frac{\cos(\theta_{N_\theta-1}) + \cos(\theta_{N_\theta})}{2} + 1 \right]. \quad (11)$$

Theta and phi are angles that define the direction of scattering in DDSCAT. Scattering is projected on to a series of scattering planes. N_ϕ is the number of scattering planes with angles ϕ . Four scattering planes were used at angles 0° , 90° , 180° and 270° . N_θ is the number of scattering angles θ within each plane. Theta ranged

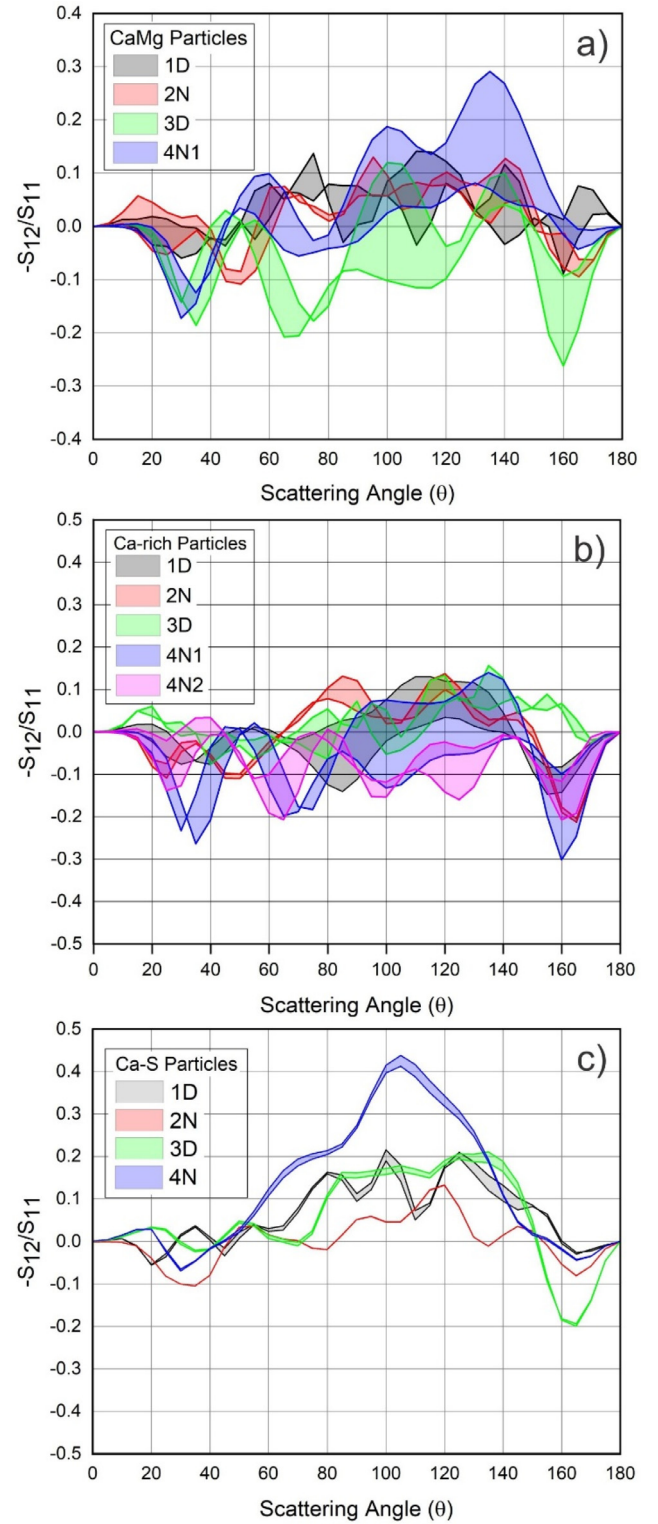


Fig. 5. Degree of linear polarization, $-S_{12}/S_{11}$, versus scattering angle for Asian dust (a and b) containing hematite as the iron phase and background marine air particles (c). Ca-S particles 1D and 2N also contained iron as hematite.

from 0° to 180° in 5° steps for a total of 37 scattering angles within each plane. Extinction efficiencies and backscatter fractions were calculated from an average of all scattering planes.

In DDA, the inter-dipole distance, d , is determined from the particle volume (vol) and the number of dipoles (N_{dp}), whereby

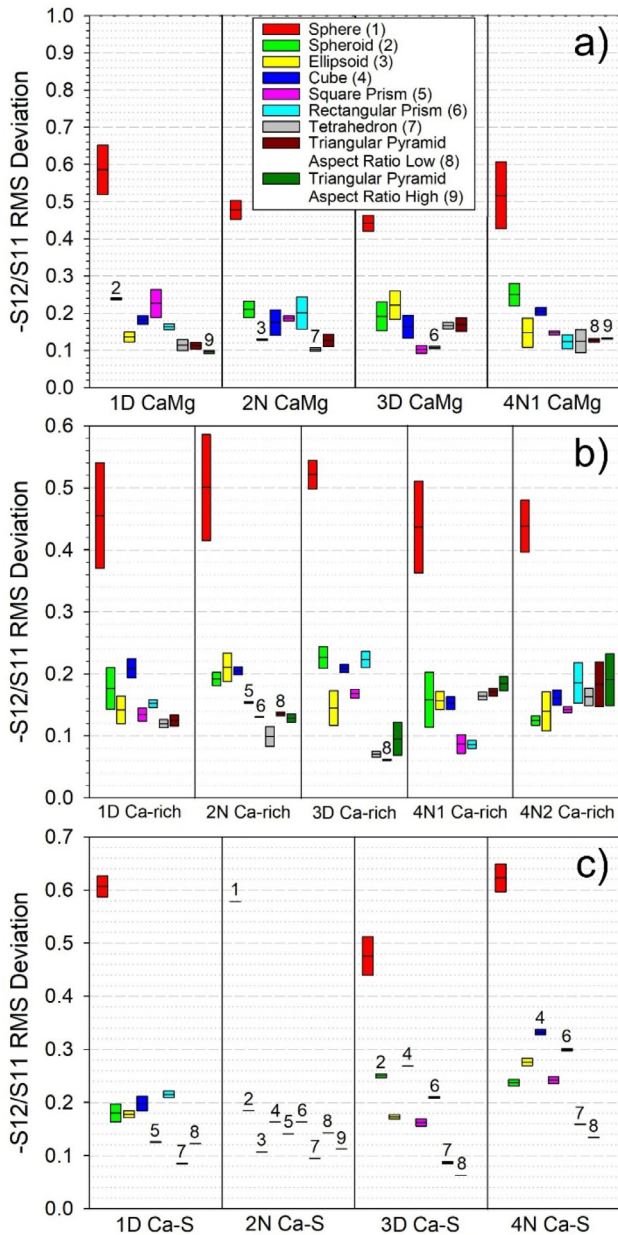


Fig. 6. Root-mean-square (RMS) deviation in $-S_{12}/S_{11}$ for geometric shapes from the respective particles containing hematite. a) and b) Asian dust particles; c) background marine air particles.

$d = (vol/N_{dp})^{1/3}$. The inter-dipole distance must be suitably minimal with respect to the incident wavelength and complex refractive index of the material. The test criterion for d is the product $|m|kd$, where $|m|$ is the absolute value of the complex refractive index. To accurately calculate the scattering phase function as well as the differential scattering cross section, $|m|kd$ should be <0.5 [53]. Table 2 shows the number of dipoles, d , $|m|$, and $|m|kd$ values for the Asian dust and background marine air particles. Minimum and maximum values for each particle in the table account for the different forms of iron in each particle (i.e., iron carbonate, hematite, magnetite) and the range of refractive indices due to the spatial orientation of the inclusion phases. Overall, $|m|kd$ values ranged from 0.218 to 0.490 and, thus, met the inter-dipole test criterion of <0.5 .

3. Results

SEM images and 3-D reconstructions of the particles in this study are shown in Fig. 2: (a) dolomite-containing CaMg Asian dust particles 1D, 2N, 3D, and 4N1, (b) calcite-containing Ca-rich Asian dust particles 1D, 2N, 3D, 4N1 and 4N2, and (c) gypsum-containing Ca-S background marine air particles 1D, 2N, 3D, and 4N. Particle diameters as size-equivalent spheres range from $0.927 \mu\text{m}$ to $1.85 \mu\text{m}$ (Table 3). With incident light for this study at $0.589 \mu\text{m}$ (λ), size parameters ($2\pi r_{\text{eff}}/\lambda$, where r_{eff} = radius of volume-equivalent sphere) ranged from 4.9 to 9.9.

The 3-D reconstructions in Fig. 2 appear to have more surface roughness than the corresponding secondary electron images. Two effects are at play. First, the higher the incident electron beam energy, the deeper primary electrons will penetrate the particle, resulting in the release of secondary electrons from deeper depths. Surface interactions then become more diluted and surface features in the images are less visible. This is the case for particles CaMg 1D and Ca-rich 1D with the primary electron beam at 20 keV, for example. The second effect is an artifact of the FIB milling process. Milling of the particle occurred in 15 nm to 20 nm steps, which resulted in surfaces having a slight terrace-like appearance in the 3-D reconstructions.

Table 3 shows the maximum lengths, 3-D aspect ratios, and volumes of the particles along with their diameters. From the top-down views of the 3-D reconstructions and electron images in Fig. 2, shapes and surface features of the reconstructions closely match the particles. All the Asian dust particles studied here contained iron; however, the identity of the iron species was inconclusive [44]. While iron oxides such as magnetite and hematite may absorb strongly in the visible and affect single scattering albedo, iron carbonates such as ankerite absorb little in the visible [57]. To study how extinction and backscattering of the particles and geometric shapes might vary with a minor iron oxide or carbonate phase, we calculated optical properties for the particles and shapes with magnetite, hematite, or iron carbonate. For the iron carbonate in the CaMg particles ankerite ($\text{CaFe}(\text{CO}_3)_2$) was used; for the Ca-rich particles siderite ($\text{Fe}(\text{CO}_3)$) was used. In contrast to the Asian dust, the Ca-S particles had little or no iron. When present, iron was included as hematite. Tables 4 and 5 show the mineral components in the Asian dust and Ca-S particles, respectively, and their volume percent.

3.1. Scattering intensity

As an indicator of scattering intensity, S_{11} versus scattering angle is analogous to the phase function. Fig. 3 shows the angular scattering intensity for the 13 particles with hematite as the iron phase. Intensity is the highest in the forward-scattering hemisphere, 0° to 90° , as expected. In addition, Fig. 3 shows how scattering varies for each particle over the range of refractive indices by implementing upper and lower refractive index limits to account for composition heterogeneity. The result is a series of ribbon-like plots where the ribbons get wider at scattering angles (θ) $>90^\circ$. Scattering intensity only appears to be more variable for backward-scattered light ($>90^\circ$) in Fig. 3 because the y-axis is logarithmic.

There is, however, a difference in scattering variability between the Asian dust (Figs. 3a and b) and background marine air particles (Fig. 3c). The Ca-S plot is less “ribbon-like” because there is less variation in the upper and lower limits to the refractive indices (Table 1). The difference between the Asian dust and background marine air particles here may be due to heterogeneity. Among the Ca-S particles in Table 5, gypsum has a much larger volume on average (89.6%) than either dolomite (65.8%) in the CaMg particles or calcite (59.2%) in the Ca-rich particles (Table 4). Thus, the Ca-S

Table 2
Number of Dipoles (N_{dp}), Inter-dipole Distance (d), Absolute Complex Refractive Index ($|m|$), and the $|m|kd$ Test Criterion.

| Particle | | Number of dipoles (N_{dp}) | Inter-dipole distance (d , μm) | $ m $ ¹ | $ m kd$ ¹ |
|----------|---------|--------------------------------|---|--------------------|----------------------|
| CaMg | 1D | 167,726 | 0.0271 | 1.502 1.673 | 0.433 0.483 |
| | 2N | 186,775 | 0.0213 | 1.503 1.656 | 0.342 0.377 |
| | 3D | 144,051 | 0.0149 | 1.502 1.665 | 0.240 0.265 |
| | 4N1 | 165,470 | 0.0136 | 1.503 1.658 | 0.218 0.241 |
| Ca-rich | 1D | 176,707 | 0.0142 | 1.498 1.647 | 0.227 0.250 |
| | 2N | 173,266 | 0.0178 | 1.515 1.573 | 0.287 0.298 |
| | 3D | 159,660 | 0.0273 | 1.508 1.681 | 0.440 0.490 |
| | 4N1 | 171,313 | 0.0137 | 1.499 1.636 | 0.219 0.239 |
| Ca-S | 4N2 | 232,605 | 0.0150 | 1.501 1.642 | 0.240 0.262 |
| | 1D | 157,025 | 0.0214 | 1.523 1.542 | 0.347 0.352 |
| | 2N | 170,584 | 0.0165 | 1.524 1.542 | 0.268 0.271 |
| | 3D | 170,330 | 0.0178 | 1.521 1.536 | 0.289 0.292 |
| 4N | 166,444 | 0.0160 | 1.521 1.538 | 0.260 0.263 | |

¹ Range of values covers the range of refractive indices for particles with magnetite, hematite, ankerite (CaMg particles), or siderite (Ca-rich particles).

Table 3
Particle Dimensions, 3-D Aspect Ratio, and Volume.

| Particle | | Diameter ¹ (μm) | Maximum Length (μm) | 3-D Aspect Ratio | Volume (μm^3) |
|----------|------|---|----------------------------------|------------------|----------------------------|
| CaMg | 1D | 1.85 | 4.19 | 2.28 | 3.32 |
| | 2N | 1.51 | 2.26 | 1.68 | 1.81 |
| | 3D | 0.97 | 1.34 | 1.35 | 0.48 |
| | 4N1 | 0.93 | 2.05 | 1.88 | 0.42 |
| Ca-rich | 1D | 0.99 | 2.65 | 2.36 | 0.51 |
| | 2N | 1.23 | 1.63 | 1.56 | 0.97 |
| | 3D | 1.84 | 2.57 | 1.57 | 3.26 |
| | 4N1 | 0.94 | 1.12 | 1.45 | 0.44 |
| Ca-S | 4N2 | 1.14 | 1.68 | 1.50 | 0.78 |
| | 1D | 1.43 | 1.68 | 2.05 | 1.54 |
| | 2N | 1.13 | 1.65 | 1.75 | 0.76 |
| | 3D | 1.23 | 1.38 | 2.07 | 0.97 |
| 4N | 1.09 | 1.41 | 2.07 | 0.68 | |

¹ For volume-equivalent sphere.

Table 4
Volume Percent of Mineral Phases in Asian Dust Particles.

| CaMg | Mineral Phase | Volume (%) | | | Ca-rich | Mineral Phase | Volume (%) | | |
|------------|------------------|-------------|-------------|-------------|------------------|-----------------------------|-------------|-------------|-------------|
| | | Magnetite | Hematite | Ankerite | | | Magnetite | Hematite | Siderite |
| 1D | Dolomite | 80.5 | 80.5 | 78.9 | 1D | Calcite | 74.4 | 74.4 | 74.9 |
| | Magnesite | 11.2 | 11.3 | 11.8 | | Albite/anorthite/orthoclase | 13.8 | 13.8 | 13.9 |
| | Montmorillonite | 6.49 | 6.49 | 6.47 | | Ammonium sulfate | 7.32 | 7.32 | 5.63 |
| | Ammonium sulfate | 1.44 | 1.44 | 1.43 | | Magnesite | 3.40 | 3.40 | 3.42 |
| | Iron phase | 0.30 | 0.31 | 1.41 | | Iron phase | 1.11 | 1.13 | 2.19 |
| 2N | Dolomite | 64.7 | 64.7 | 61.5 | 2N | Gypsum | 65.4 | 65.4 | 64.9 |
| | Montmorillonite | 16.2 | 16.2 | 16.1 | | Calcite | 23.1 | 23.1 | 22.9 |
| | Magnesite | 12.6 | 12.6 | 13.7 | | Albite/anorthite/orthoclase | 9.10 | 9.11 | 9.04 |
| | Ammonium sulfate | 5.80 | 5.81 | 5.77 | | Magnesite | 1.55 | 1.55 | 1.54 |
| | Iron phase | 0.64 | 0.65 | 2.96 | | Iron phase | 0.80 | 0.81 | 1.55 |
| 3D | Dolomite | 77.1 | 77.1 | 74.7 | 3D | Calcite | 67.0 | 67.0 | 64.4 |
| | Montmorillonite | 10.0 | 10.0 | 9.95 | | Albite/anorthite/orthoclase | 16.3 | 16.3 | 15.7 |
| | Magnesite | 8.13 | 8.12 | 8.96 | | Iron phase | 4.26 | 4.33 | 8.03 |
| | Ammonium sulfate | 4.24 | 4.25 | 4.22 | | Gypsum | 7.83 | 7.84 | 7.53 |
| | Iron phase | 0.47 | 0.48 | 2.20 | | Magnesite | 3.98 | 4.15 | 3.98 |
| 4N1 | phase | | | | Rhodochrosite | 0.38 | 0.40 | 0.38 | |
| | Dolomite | 40.9 | 40.9 | 36.9 | 4N1 | Calcite | 71.3 | 71.3 | 70.8 |
| | Magnesite | 20.0 | 20.1 | 21.4 | | Gypsum | 19.7 | 19.7 | 19.6 |
| | Montmorillonite | 19.9 | 19.9 | 19.7 | | Quartz/anorthite | 6.32 | 6.32 | 6.27 |
| | Gypsum | 18.3 | 18.3 | 18.2 | | Magnesite | 1.94 | 1.94 | 1.92 |
| Iron phase | 0.83 | 0.84 | 3.83 | Iron phase | | 0.73 | 0.74 | 1.41 | |
| 4N2 | | | | 4N2 | Calcite | 60.3 | 60.3 | 60.1 | |
| | | | | | Magnesite | 15.8 | 15.8 | 15.8 | |
| | | | | | Quartz/feldspar | 11.5 | 11.5 | 11.4 | |
| | | | | | Ammonium sulfate | 12.1 | 12.1 | 12.0 | |
| | | | | | Iron phase | 0.36 | 0.37 | 0.71 | |

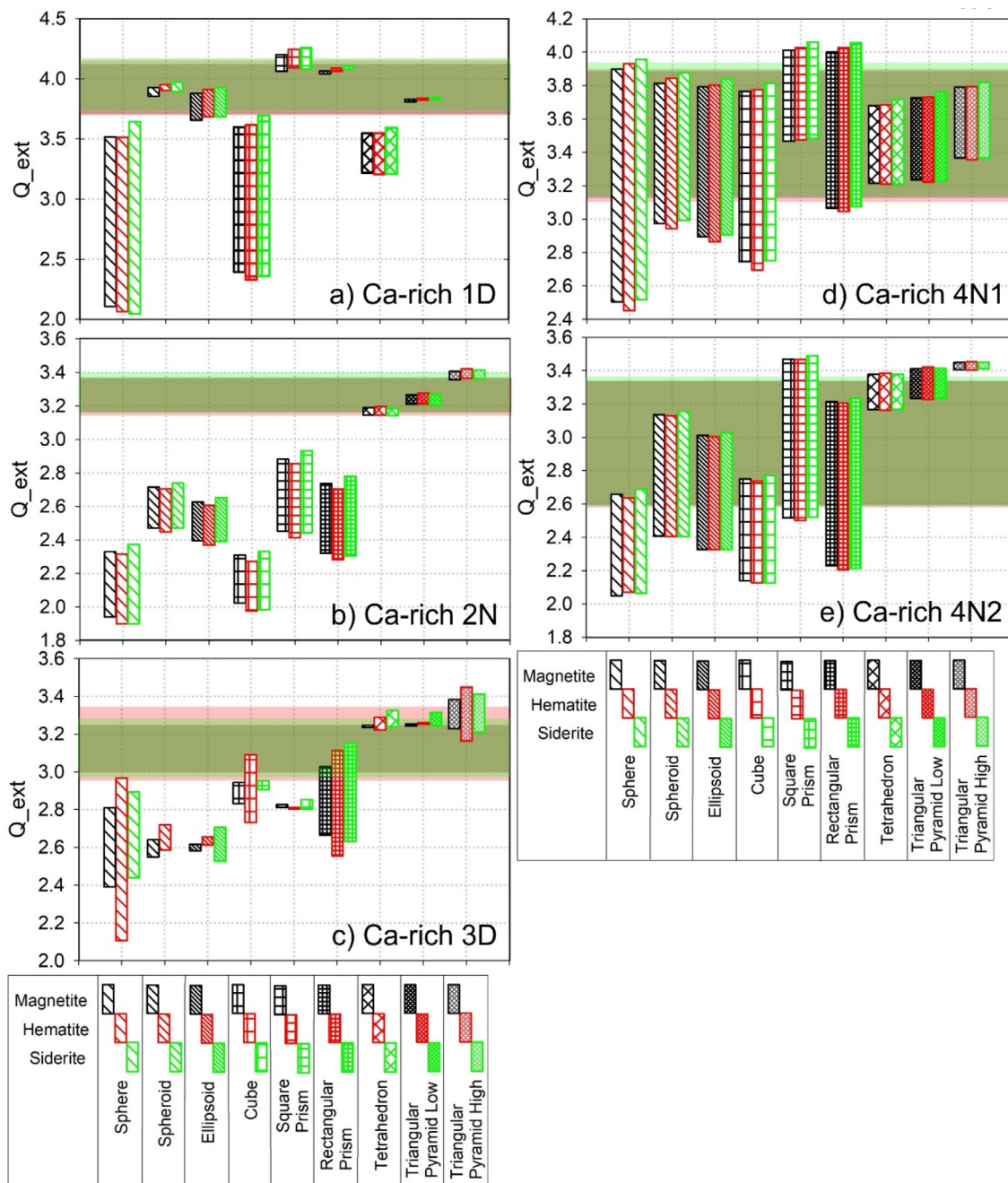


Fig. 7. Range of extinction efficiencies for geometric shapes and Ca-rich particles with the iron phase as light-absorbing magnetite (black) or hematite (red), or non-absorbing siderite (green). Shaded areas show ranges for the particle with the different iron phases. Triangular pyramid low and triangular pyramid high have aspect ratios that bracket the aspect ratio of the particle (see Table 3). For particle 1D, the triangular pyramid aspect ratio (low) was close to the aspect ratio for the particles.

particles are more homogeneous than the Asian dust particles, and variation in the spatial orientation of the minor mineral phases in the Ca-S particles has less of an effect on the scattering intensity.

We now look at how scattering intensity compares between the particles and geometric shapes. As a measure of how close the scattering intensity for the shapes matches the particles, we employ the root-mean-square deviation (RMSD) in S_{11} for the shape and particle between scattering angles 30° and 180° , as shown in Fig. 4:

$$S_{11} \text{ RMSD} = \left(\frac{\sum_{30^\circ}^{180^\circ} (S_{11_{model}} - S_{11_{particle}})^2}{n} \right)^{1/2}. \quad (12)$$

Here, $n=31$, the number of angles from 30° to 180° in 5° steps. The extent of the bars in Fig. 4 is due to the application of upper and lower refractive index limits. The horizontal line within each bar is the midpoint. RMSD is determined between scattering angles 30° and 180° rather than 0° and 180° because typically $(S_{11_{model}} - S_{11_{particle}})^2$ is excessively large from 0° to 30° and the extent of the bars in Fig. 4 can vary by several fold.

The large variability in S_{11} RMSD values for individual shapes in Fig. 4 is due to the enhanced effect of disparate upper and lower refractive index limits. The square prism for the Ca-rich 3D and the sphere for the Ca-rich 4N2 particle exhibit the largest RMSD variability. In both cases, the greatest S_{11} disparity in shape versus particle occurred with the upper refractive index limit (Table 1).

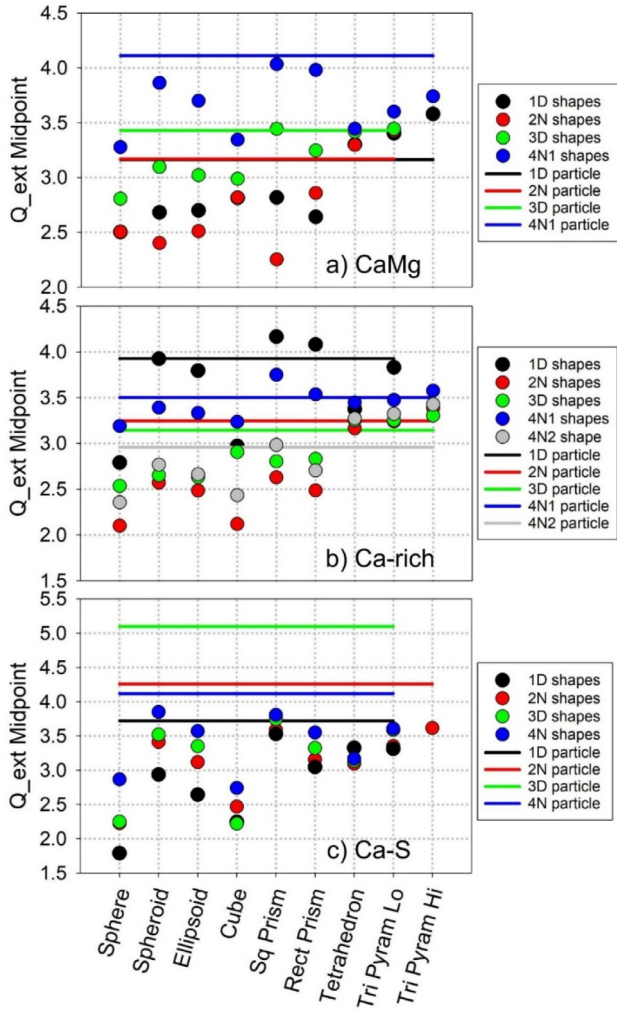


Fig. 8. Midpoints of extinction efficiencies for geometric shapes and particles with hematite as the iron phase. a) and b) Asian dust; c) background marine air particles. For particles CaMg 2N, CaMg 3D, Ca-rich 1D, Ca-S 1D, Ca-S 3D, and Ca-S 4N the triangular pyramid aspect ratio (low) was close to the aspect ratio for the particles, therefore, the triangular pyramid aspect ratio (high) was not considered.

Table 5
Volume Percent of Mineral Phases in Ca-S Background Marine Air Particles.

| | Mineral Phase | Volume (%) |
|----|---------------------|------------|
| 1D | Gypsum | 91.5 |
| | Calcite | 4.13 |
| | Quartz | 1.65 |
| | Albite | 0.89 |
| | Magnesite | 1.49 |
| 2N | Hematite | 0.30 |
| | Gypsum | 90.8 |
| | Calcite | 4.56 |
| | Albite | 3.45 |
| 3D | Magnesite | 0.78 |
| | Hematite | 0.42 |
| | Gypsum | 85.7 |
| | Calcite | 1.32 |
| | Albite (K-feldspar) | 11.0 |
| 4N | Magnesite | 1.96 |
| | Hematite | 0 |
| | Gypsum | 90.5 |
| | Calcite | 3.33 |
| | Quartz | 4.39 |
| | Anorthite | 0.49 |
| | Magnesite | 1.30 |
| | Hematite | 0 |

The disparity was largest at scattering angles >160° and >170°, thus, primarily affecting backscattering as shown for the Ca-rich 3D square prism and Ca-rich 4N2 sphere, respectively, in Figs. S1 and S2 of *Supplementary Material*.

We might expect higher-order geometric shapes (e.g., 3-axis rectangular prism versus 2-axis square prism and 2-axis square prism versus cube) to exhibit a lower RMSD because they should approximate the shape of the actual particles more closely than lower-order shapes. This is best exemplified by the particle CaMg 1D shapes in Fig. 4a. Here, the RMSD midpoints are unequivocally lower for the ellipsoid versus spheroid and spheroid versus sphere; for the rectangular prism versus square prism and square prism versus cube; and for the triangular pyramid versus tetrahedron. Among the ellipsoid group shapes, RMSD for spheroids is lower than for spheres for 12 of the 13 particles; RMSD for ellipsoids is lower than for spheres in all cases.

Nevertheless, we cannot necessarily expect the scattering intensity of a 3-axis shape to be closer to the particle than a 2-axis shape. RMSD for ellipsoids is lower than spheroids in only 8 of 13 particles. For the cuboid group, RMSD for rectangular prisms is lower than cubes in 12 of 13 particles. However, RMSD for rectangular prisms is lower than square prisms in only 7 of 13 particles. RMSD for square prisms is lower than cubes in 9 of 13 particles. Thus, scattering intensity by higher-order shapes is not always closer to the actual particles than scattering intensity by lower-order shapes. In a comparison with feldspar particles [27], the phase function of elongated spheroids was found to be a better match than less-elongated spheroids suggesting in this case that elongated spheroids performed better than would ellipsoids with less disparate dimensions.

3.2. Degree of linear polarization

Fig. 5 shows the degree of linear polarization for the 13 particles with hematite as the iron phase. The ribbon plots show the extent that linear polarization for each particle varies over the range of refractive indices used to account for composition heterogeneity. For several of the Asian dust particles, e.g., CaMg 3D and CaMg 4N1, Ca-rich 1D, and Ca-rich 4N1, greater variability in linear polarization due to composition heterogeneity occurs at scattering angles of around 80° and higher.

As observed for S_{11} (Fig. 3), Fig. 5 shows much greater variability in the linear polarization of each Asian dust particle due to composition heterogeneity compared to the background marine air particles. As noted previously, Ca-S particles are more homogeneous than the Asian dust particles. It appears that variation in the spatial orientation of the minor mineral phases in the Ca-S particles has less of an effect on the degree of linear polarization than on the more heterogeneous Asian dust particles.

As with scattering intensity, we compared the degree of linear polarization between the particles and shapes. Analogous to Eq. (12), we calculated the root-mean-square deviation (RMSD) in $-S_{12}/S_{11}$ for the shape and particle between scattering angles 30° and 180°, as shown in Fig. 6:

$$-S_{12}/S_{11} \text{ RMSD} = \left(\frac{\sum_{30^\circ}^{180^\circ} \left(\left(-\frac{S_{12}}{S_{11}} \right)_{\text{model}} - \left(-\frac{S_{12}}{S_{11}} \right)_{\text{particle}} \right)^2}{n} \right)^{1/2} \quad (13)$$

RMSD is calculated here between scattering angles 30° and 180° to maintain comparability in RMSD values for the scattering intensity.

As Fig. 6 shows, $-S_{12}/S_{11}$ RMSD for spheres is much larger in all cases than for other shapes. The contrast in RMSD between the

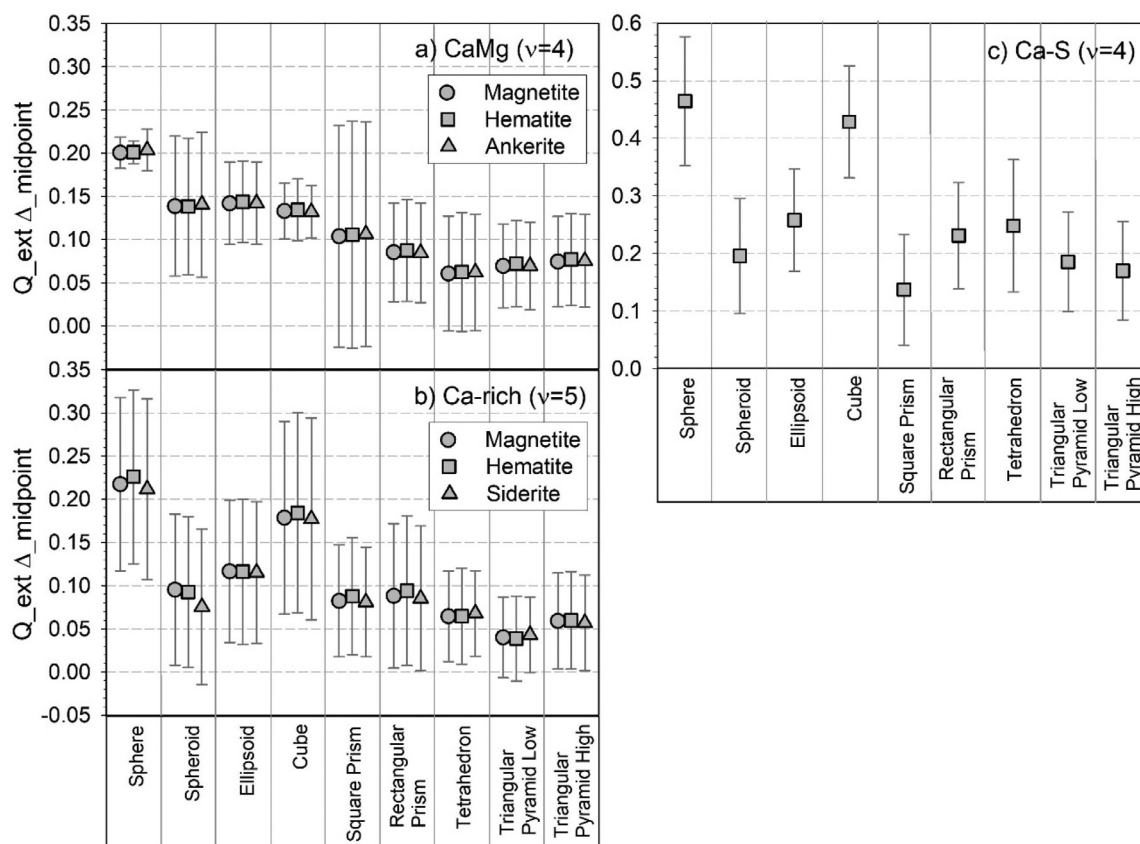


Fig. 9. Average of the normalized differences (Δ) in midpoints for the extinction efficiency for geometric shapes from those of particles. a) and b) Asian dust; c) background marine air particles. Error bars indicate standard deviation. ν corresponds to the number of particles. .

sphere and other shapes for the degree of linear polarization is much larger than the RMSD contrast between the sphere and other shapes for the scattering intensity (Fig. 4).

Among shapes other than the sphere, the RMSD midpoint (horizontal line in each bar) is lower for ellipsoids than for spheroids in 9 of 13 particles, comparable to the number of ellipsoids with lower RMSD midpoints than spheroids for S_{11} (Fig. 4). For the cuboid group, $-S_{12}/S_{11}$ RMSD midpoints for rectangular prisms are lower than for cubes in 8 of 13 particles. However, midpoints for rectangular prisms are lower than for square prisms in only 4 of 13 particles. Thus, consistent with scattering intensity, the degree of linear polarization by higher-order shapes was not always closer to the actual particles than linear polarization by lower-order shapes. Notably however, $-S_{12}/S_{11}$ RMSD midpoints for the tetrahedra and triangular pyramids in Fig. 6 are lower than for the spheroids, ellipsoids, cubes, and square prisms in 9 of 13 particles.

3.3. Extinction efficiency

In Fig. 7 we show how the geometric shapes compare with the Ca-rich particles with different forms of the minor iron phase: magnetite (black), hematite (red), or siderite (green). Similar comparisons are shown for the CaMg and Ca-S particles in Figs. S3 and S4 in *Supplementary Material*. The bars indicate the range of extinction efficiencies for the geometric shapes from applying the upper and lower refractive index limits. The colored shaded areas in each plot (black, red, and green corresponding to magnetite, hematite, and siderite) indicate the range in extinction efficiencies for the particles. Overlap of the shaded areas shows how extinction efficiencies for a particle with different iron phases compare. We ob-

serve how well the geometric shapes match the particles in each case from how closely the bars overlap the shaded areas.

As the shaded areas in Fig. 7 show, the range of extinction efficiencies among the particles due to variation in the spatial arrangement of the phases can be quite different. For example, extinction for particle Ca-rich 2N with hematite varies by 7% (Fig. 7b), but by 23% for particle 4N2 (Fig. 7e). Similarly, the range of extinction efficiencies among the shapes associated with a particle can be quite different. In Fig. 7e, extinction for the triangular pyramid-high with hematite varies by 2%, but by 31% for the rectangular prism.

In addition, there is extensive overlap of the shaded areas in Fig. 7 for each particle in general. This indicates that the type of the iron phase in the Asian dust particles has little effect on extinction. Similarly, the extinction efficiencies of the geometric shapes associated with each particle vary little with the type of iron phase. An exception, however, is particle Ca-rich 3D in Fig. 7c. The iron content of Ca-rich 3D is 3.6 to 14 times higher than the iron content of the other Asian dust particles. The siderite volume for Ca-rich 3D is 8.03% (Table 4) while the average iron carbonate volume for the other Asian dust particles (Ca-rich and CaMg) is $(2.04 \pm 0.99)\%$ ($\bar{x} \pm s$).

Another observation from Fig. 7 is that higher-order geometric shapes appear to more closely approximate extinction for particles with a large aspect ratio. Others have shown that distributions of spheroids with large aspect ratios, particularly prolate spheroids, tend to better match the measured phase function of particle ensembles [27]. Ca-rich 1D in Fig. 2b has an aspect ratio 2.36 (Table 3). Long and conical, the particle resembles a prolate spheroid. As shown in Fig. 7a, shapes with two or three axes (spheroid, ellipsoid, square prism, rectangular prism, and triangular

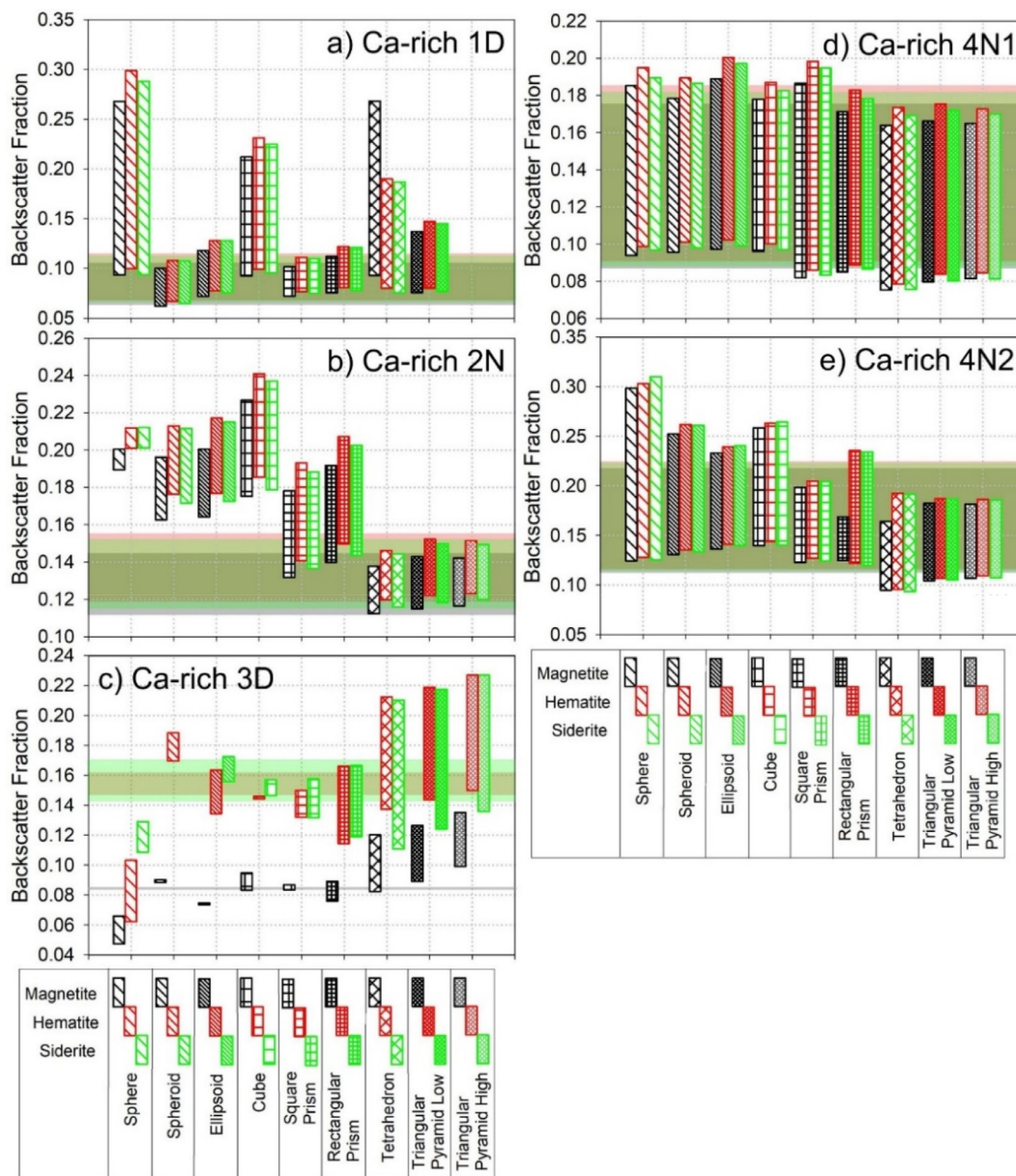


Fig. 10. Range of backscatter fractions for geometric shapes and Ca-rich particles with the iron phase as light-absorbing magnetite (black) or hematite (red), or non-absorbing siderite (green). Shaded areas show ranges for the particle with different iron phases. Triangular pyramid low and triangular pyramid high have aspect ratios that bracket the aspect ratio of the particle (see Table 3). For particle 1D, the triangular pyramid aspect ratio (low) was close to the aspect ratio for the particles.

pyramid) come much closer to the extinction efficiency of the particle than the single-axis shapes. However, we cannot assume that higher-order shapes better approximate particles with large aspect ratios. Particle CaMg 1D in Fig. 2a, for example, also has a large aspect ratio (2.28). Fig. S1a in *Supplementary Material* shows that while the spheroid and ellipsoid are closer than the sphere to the CaMg 1D particle, the cube is actually closer than the rectangular prism to the particle.

Also for particle CaMg 1D in Fig. S1a, the extinction efficiency for the cube is closer to the particle than either the spheroid or ellipsoid. In contrast, the spheroid and ellipsoid are far closer than the cube to the extinction efficiency of Ca-rich 1D. Sphericity here may be a factor. There is only a 4% difference in the aspect ratios between CaMg 1D (2.28) and Ca-rich 1D (2.36). However, Ca-rich 1D has a sphericity of 0.59 while CaMg 1D has a sphericity of 0.50, a difference of 17%. Thus, CaMg 1D is less spherical than Ca-rich 1D, and this may explain why the cube more closely approximates extinction for CaMg 1D than the spheroid and ellipsoid.

A better understanding of the geometric shapes and respective particles can be drawn from the midpoints of the extinction efficiency ranges, which are shown in Fig. 8. Circles are the midpoints for the geometric shapes and horizontal lines are the midpoints for the particles. The iron phase here is hematite. Close inspection of the midpoint plots reveals that the geometric shapes overall tend to underestimate the particles' extinction efficiency. For the CaMg particles, 26 of 34 shapes underestimated particle extinction (6 of 9 shapes for particle 1D, 6 of 8 shapes for 2N, 5 of 8 shapes for 3D, and 9 of 9 shapes for 4N1). Thus, 76% of the geometric shapes underestimated extinction for the CaMg particles. For the Ca-rich particles, 28 of 44 shapes underestimated particle extinction (5 of 8 shapes for particle 1D, 7 of 9 for 2N, 6 of 9 for 3D, 5 of 9 for 4N1, and 5 of 9 for 4N2). Thus, 64% of the geometric shapes for the Ca-rich particles underestimated extinction. In contrast to the Asian dust particles, all geometric shapes underestimated extinction for the Ca-S particles.

The extent that Asian dust extinction is underestimated is not the same, however, among the shape groups. For the CaMg particles, extinction was underestimated by all ellipsoid group shapes, 92% of the cuboid shapes, but only 30% of the pyramid shapes. For the Ca-rich particles, extinction was underestimated by 93% of the ellipsoid group shapes, 67% of the cuboid shapes, and 29% of the pyramid shapes. Thus, the ellipsoid and cuboid groups tended to underestimate extinction for the Asian dust particles while the pyramid shapes tended to overestimate extinction. Shapes in all three groups underestimated extinction for the background marine air particles.

Another observation from Fig. 8 is that the pyramid shapes generally exhibit less variation in the extinction efficiency, particularly the tetrahedron, compared to variation among the other shapes. For example, the ratio of the range of Q_{ext} midpoints for the tetrahedra to the range of midpoints for the CaMg particles in Fig. 8a is 0.16. The ratio of Q_{ext} midpoint ranges for the spheroids and CaMg particles is 1.5. Likewise, the ratio of midpoint ranges for the tetrahedra and Ca-rich particle in Fig. 8b is 0.28 while the ratio of midpoint ranges for the spheroids and Ca-rich particles is 1.4. The tetrahedra versus spheroids in Fig. 8c for the Ca-S particles exhibit a similar contrast. Thus, Q_{ext} variation for the tetrahedra is much smaller than the variation for particles while the variation for the spheroids is closer to that for the particles.

To quantify how well the geometric shapes performed in approximating the extinction efficiency, we applied a delta function that is the normalized difference in the midpoints $Q_{\text{ext_midpt_shape}}$ and $Q_{\text{ext_midpt_particle}}$ of the extinction efficiencies for shape and particle:

$$Q_{\text{ext}} \Delta_{\text{midpt}} = \text{abs} \left[\frac{Q_{\text{ext_midpt_shape}} - Q_{\text{ext_midpt_particle}}}{Q_{\text{ext_midpt_particle}}} \right]. \quad (14)$$

Fig. 9 shows the overall performance for extinction efficiency as the average of the delta midpoint values. Error bars are standard deviations. As mentioned above, the type of iron phase in the Asian dust particles had a negligible effect overall on how well the shapes approximated the extinction efficiency. For CaMg and Ca-rich particles, the delta midpoint average is smallest for the tetrahedron and triangular pyramid shapes, and thus, these shapes more closely approximated extinction for the Asian dust. For the Ca-S particles, delta midpoint average is the smallest for the square prism; however, the triangular pyramid also performed well as did the spheroid. The sphere performed the worst for approximating extinction in all three cases.

3.4. Backscatter fraction

The effect of the different iron phases on the backscatter fraction for the Ca-rich particles and the geometric shapes is shown in Fig. 10. Similar comparisons for the CaMg and Ca-S geometric shapes and particles are shown in Figs. S5 and S6 in *Supplementary Material*. As in Fig. 7, the bars indicate the range of the backscatter fractions for the geometric shapes and the shaded areas indicate the range for the particles. As we observed with extinction, the higher-order shapes in Fig. 10a more closely approximate the backscatter fraction for particle Ca-rich 1D with its large aspect ratio and nearly spheroidal shape.

Comparing Figs. 10 and 7, the different iron phases in the geometric shapes have a greater effect on the backscatter fraction than on extinction. The effect is obvious for particle 3D (Fig. 10c), which has the highest iron content as mentioned previously. The colored shaded areas in Fig. 10c show that the backscatter fraction for the particle is substantially smaller with magnetite (gray area with midpoint 0.084) than with either hematite (red area with midpoint 0.155) or siderite (green area with midpoint 0.157). In this case, the

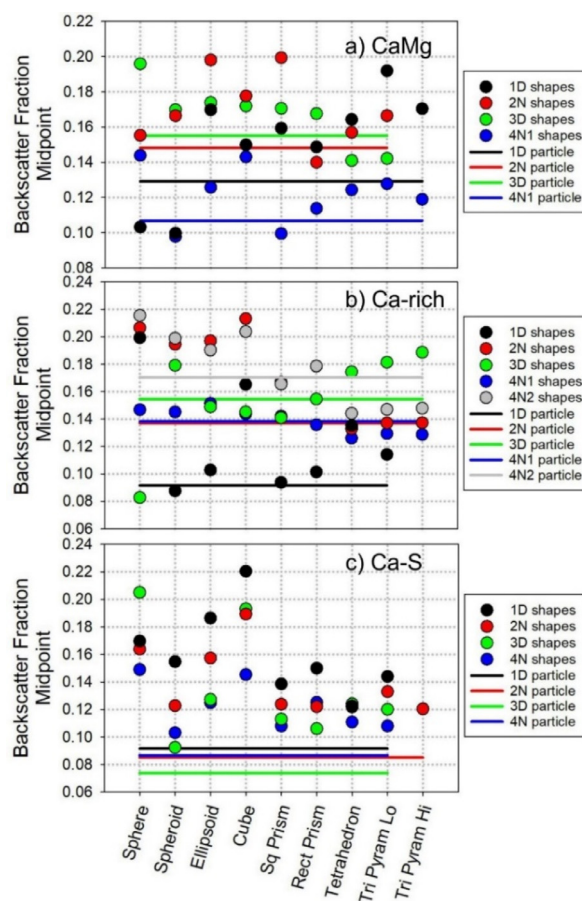


Fig. 11. Midpoints of the backscatter fractions for geometric shapes and particles with hematite as the iron phase. a) and b) Asian dust; c) background marine air particles.

backscatter fraction for the particle is largely affected by the magnitude of the imaginary part of the complex refractive index for the particle. The particle's imaginary part with magnetite is 0.023 (Table 1), a factor of 10 larger than with hematite (0.00228). The real part of the complex refractive index shown in Table 1 likely contributes little to variation in the backscatter fraction for particle Ca-rich 3D because the variation in the real refractive index for the particle with different iron phases is minimal.

The midpoints of the backscatter fraction ranges, shown in Fig. 11, provide further insight into the backscatter fractions for the geometric shapes and particles. Close inspection of Fig. 11 reveals that in contrast to extinction, the shapes tend to overestimate the backscatter fraction of the particles. This is clearly the case for the Ca-S background marine air particles (Fig. 11c). Here, all shapes overestimated the backscatter fraction.

For the Asian dust CaMg particles, 27 of 34 shapes (79%) overestimated the backscatter fraction (7 of 9 shapes for particle 1D, 7 of 8 shapes for 2N, 6 of 8 shapes for 3D, and 7 of 9 shapes for 4N1). For the Ca-rich particles, 26 of 44 shapes (59%) overestimated the backscatter fraction (6 of 8 shapes for particle 1D, 6 of 9 shapes for 2N, 4 of 9 for 3D, 5 of 9 for 4N1, and 5 of 9 for 4N2).

Among the shape groups, the backscatter fraction for the CaMg particles was overestimated by 75% of the ellipsoid group shapes, 83% of the cuboid shapes, and 80% of the pyramid shapes. For the Ca-rich particles, the backscatter fraction was overestimated by 80% of ellipsoid group shapes, 67% of cuboid shapes, but only 36% of pyramid shapes. Overall, shapes in the ellipsoid and cuboid groups tended to overestimate the Asian dust backscatter frac-

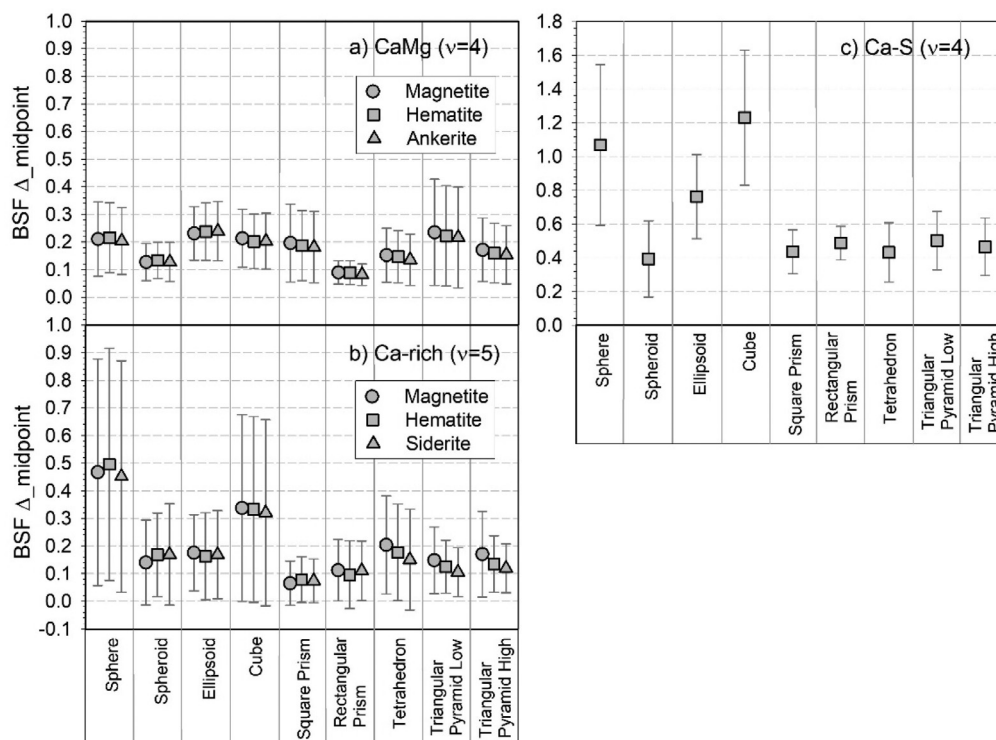


Fig. 12. Average of the normalized differences (Δ) in midpoints for the backscatter fraction for shapes from those of particles. a) and b) Asian dust; c) background marine air particles. Error bars indicate standard deviation. ν corresponds to the number of particles.

tion to a greater extent than did the pyramid shapes. The pyramid shapes tended to underestimate or closely approximated the backscatter fraction for the Ca-rich particles.

To quantify how well the geometric shapes performed at approximating the backscatter fraction, we used a delta function analogous to Eq. (14):

$$BSF \Delta_{midpt} = \text{abs} \left[\frac{(BSF_{midpt_shape} - BSF_{midpt_particle})}{BSF_{midpt_particle}} \right]. \quad (15)$$

Fig. 12 shows the BSF delta midpoint averages. As in Fig. 9, the y-axes in Fig. 12a and b (CaMg and Ca-rich) are scaled the same for comparison. Fig. 12a shows that while the rectangular prism appears to have approximated the backscatter fraction slightly better than other shapes for the CaMg particles, there is nevertheless little variation among the geometric shapes. Fig. 12b shows that while the sphere and cube performed worse in approximating the backscatter fraction for the Ca-rich particles, there is little variation among the remaining geometric shapes, particularly between the 2- and 3-axis shapes. Geometric shapes for the Ca-S particles performed like the Ca-rich particles. Except for the ellipsoid, there is little variation in how closely the 2- and 3-axis shapes approximated the backscatter fraction.

3.5. Surface roughness

The particles in Fig. 2 have surface features that are often described as surface roughness. As explained previously, electron penetration during SEM imaging and ion-beam milling of the particle can affect apparent surface smoothing. The true roughness is important because increased surface roughness results in increased particle surface area which generally results in increased scattering. For particles with very large size parameters, most of the total scattering may come from surface roughness [58]. Increased surface roughness was shown to only slightly affect single scattering

albedo [38], suggesting that surface roughness increases absorption as well as scattering, and thus, extinction is increased comparably with surface roughness. An important question in this work is how much of extinction efficiency and the backscatter fraction is due to surface roughness.

The use of Avizo to create the 3-D spatial representations of particles allowed us to remove surface roughness without significantly changing the particle volume. The procedure is based on a generalized marching cubes algorithm for creating a smooth surface [59]. In the algorithm, surface voxels in the 3-D representation are treated as cubes. An isosurface is created that lies above or below the vertices of the cube. The extent to which the cube vertices influence the isosurface depends on weights or probabilities that are calculated separately from the marching cubes algorithm [60]. The weights are translated in Avizo to smoothing levels from 1 to 9.

Table 6 shows how smoothing at the highest level (9) changed the number of dipoles, volume, and inter-dipole distance for each particle. For all particles except Ca-S 2N, smoothing decreased the number of dipoles by < 5%. The change in volume, however, was negligible, < 1% among all particles. Rather than change volume, the marching cubes algorithm adjusted the inter-dipole distance, increasing it slightly for all particles except Ca-S 2N. In DDSCAT, coordinates of the voxels from the 3-D spatial models of the smoothed particles accounted for the change in the inter-dipole distance. Since the change in particle volume with smoothing was negligible, particle diameters as volume-equivalent spheres (Table 3) were left unchanged.

Fig. 13 shows a selection of particles and the visual effect of smoothing at levels 3, 6, and 9. In general, particle shape did not change after smoothing. Smoothing revealed that, overall, surface roughness contributed a minor amount to the extinction efficiency as observed in Fig. 15. Based on the highest smoothing level (9), surface roughness accounted for $(3.2 \pm 2.9) \%$ ($\bar{x} \pm s$) of total ex-

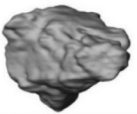
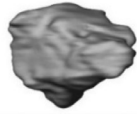
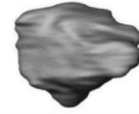
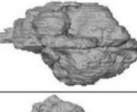
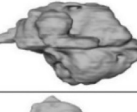
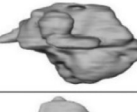
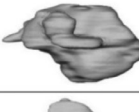
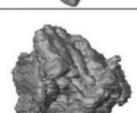
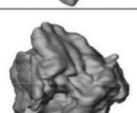
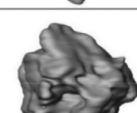
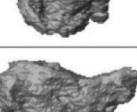
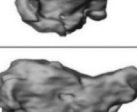
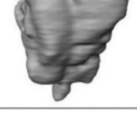
| | Native Particle | Smoothing Level 3 | Smoothing Level 6 | Smoothing Level 9 |
|------------|---|---|--|---|
| CaMg 3D |  |  |  |  |
| CaMg 4N1 |  |  |  |  |
| Ca-rich 1D |  |  |  |  |
| Ca-rich 2N |  |  |  |  |
| Ca-rich 3D |  |  |  |  |
| Ca-S 1D |  |  |  |  |
| Ca-S 4N |  |  |  |  |

Fig. 13. Effect of smoothing selected particles to remove surface roughness. Smoothing levels are weights to adjust the generalized marching cubes algorithm [59,60] used by Avizo to smooth a surface. Level 9 is maximum smoothing.

tion for the CaMg and Ca-rich Asian dust particles and $9.61 \pm 3.2\%$ of total extinction for the Ca-S background marine air particles. Among the CaMg particles, surface roughness of particle 3D contributed the least to total extinction (1%) while surface roughness of particle 4N1 contributed the most (5%). For the Ca-rich particles, surface roughness of particle 1D contributed the least to extinction (1%); particle 2N contributed the most (10%). Surface roughness of particle Ca-S 1D contributed the least to extinction (6%) among the Ca-S particles; particle 4N contributed the most (13%).

While surface roughness increased particle extinction in this study as expected, surface roughness invariably decreased the backscatter fraction as observed in Fig. 16. Others have shown that surface roughness causes an enhancement of the phase function at angles $>90^\circ$ [58] which suggests an increase in the backscatter fraction. In this study, surface roughness decreased the backscatter fraction to a greater extent for the Ca-S particles, by $(16.4 \pm 6.7)\%$ ($\bar{x} \pm s$), than for the Asian dust particles ($(5.2 \pm 5.0)\%$ ($\bar{x} \pm s$)). To contrast the effect among the CaMg particles, surface roughness decreased the backscatter fraction by 1.5% for particle 1D but by 11.6% for particle 4N1. Among the Ca-rich particles, the surface

roughness decreased the backscatter fraction by $< 1\%$ for particle 3D but by 15.3% for particle 2N. With the Ca-S particles, the backscatter fraction for particle 1D decreased by 6.7% but by 21% for particle 3D.

4. Discussion

It is intuitive that simple geometric particle shapes with three optimal-length axes should approximate the shape of real individual atmospheric particles better than shapes with two axes. As mentioned in section 3.1 (Fig. 4), ellipsoids were better than spheroids at approximating scattering intensity in most cases (8 of 13) and rectangular prisms were better than square prisms in most cases (7 of 13 cases). Ellipsoids were also often better than spheroids at approximating the degree of linear polarization (9 of 13 cases, Fig. 6). However, Fig 6 also shows that rectangular prisms were often no better than square prisms at approximating the degree of linear polarization.

If we compare extinction efficiencies in Fig. 8 with scattering intensity RMSD in Fig. 4, there are differences in how the higher-order geometric shapes performed versus lower-order shapes for

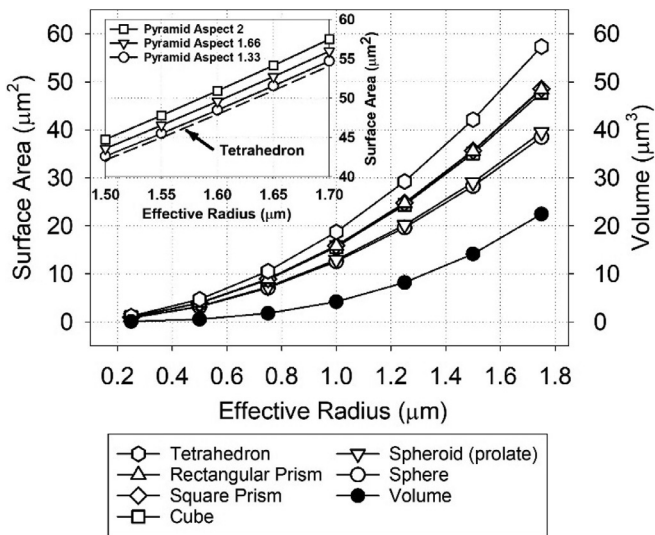


Fig. 14. Surface area versus effective radius for geometric shapes. Also plotted is volume versus effective radius.

individual particles. From the midpoints in the figures, the ellipsoids that are better than spheroids at approximating scattering intensity are not necessarily better than spheroids at approximating extinction. Examples are CaMg 1D, CaMg 4N1, Ca-rich 1D, Ca-rich 3D, and Ca-S 1D. For all these particles, the RMSD in Fig. 4 for the ellipsoid is lower than the RMSD for the spheroid as well as the sphere. However, Fig. 8 shows that the extinction efficiency for the ellipsoid in these cases is not closer to the particles than the spheroid. In the case of CaMg 2N, RMSD in Fig. 4 is much lower for the ellipsoid than the sphere, but the extinction efficiencies for the ellipsoid and sphere in Fig. 8 are about the same. We note that the scattering intensity in Fig. 4 is from the 30° angle rather than 0° whereas the extinction efficiency involves all scattering angles. Nevertheless, this discrepancy does not account for the differences in scattering intensity versus extinction with respect to the ellipsoid and spheroid shapes. The more likely reason is that extinction includes the effect of absorption, which in this case is from the hematite phase.

We now ask whether geometric shapes that provide greater surface area can account for particle surface roughness. Fig. 14 shows how the surface area and volume for the geometric shapes increase with effective radius. The incremental increase in surface area with radius is greater than the volume increase. More importantly, the incremental increase in surface

area is greater for the cube than for the sphere and for the tetrahedron than for the cube. At the same volume, a tetrahedron has one and a half times the surface area of a sphere. Thus, we might expect the pyramid group to account for more scattering due to more surface area than either the cuboid or ellipsoid group. Fig. 14 also shows that higher-order shapes within a shape group offer little additional surface area over lower-order shapes. Aspect ratio is a factor. Larger aspect ratios result in more surface area. Also, 3-axis shapes also have slightly less surface area than volume-equivalent 2-axis shapes. For example, while a spheroid has more surface area than a sphere, an ellipsoid has less surface area than a spheroid because the additional dimension makes an ellipsoid more spherical. As mentioned previously, simulated phase matrices for elongated prolate spheroids have been shown to be closer to the phase matrix for measured particles than less-elongated or more sphere-like spheroids [27,42].

Fig. 15 shows how the extinction efficiency for the geometric shapes compares with the particles as the particles are smoothed to remove surface roughness. The gradation in the extinction efficiency due to smoothing is shown by the series of horizontal lines in each plot. The black line indicates the extinction efficiency without smoothing (native particle). The two CaMg particles 3D and 4N1 (Fig. 15a and b) show the effect of contrasting contributions to extinction from surface roughness. In Fig. 15a, variation in the extinction efficiency among the ellipsoid group and cuboid shapes for particle 3D, as indicated by the shaded areas, is far larger than the decrease in extinction due to smoothing of the particle. With surface roughness contributing only 1% to extinction for particle 3D, shape matters for the most part not surface roughness. For particle 4N1 (Fig. 15b), which has 5% of its extinction from surface roughness, smoothing decreases the particle extinction efficiency sufficiently so that we see which shapes might account for surface roughness. While the shaded areas show that variation in extinction within each shape group is rather large, the square and rectangular prisms come closest to the native particle. Nevertheless, it is unlikely that geometric shape accounts for surface roughness here because the cube's extinction efficiency is far from the native particle. As Fig. 14 shows, the square and rectangular prisms have only slightly more surface area than the cube. If surface area were a factor with particle CaMg 4N1, then the cube should also be close to the particle.

The two Ca-S particles 1D and 4N in Fig. 15e and f also show the effect of contrasting contributions to the extinction efficiency from surface roughness. Particle 1D has 7% of its extinction from surface roughness while particle 4N has 20%. Here also the square prism (and spheroid in particle 4N) comes closest to approximating the particles' extinction. However, as with the CaMg particles, surface roughness is unlikely a factor for particle 4N because the

Table 6
Change in Particle Dipole Number, Volume, and Inter-dipole Distance with Maximum Smoothing.

| Particle | Number of dipoles (N_{dp}) | | Volume (μm^3) | | Inter-dipole distance (d , μm) | | |
|----------|--------------------------------|---------------------------------|----------------------------|---------------------------------|---|---------------------------------|-------|
| | | Change from native particle (%) | | Change from native particle (%) | | Change from native particle (%) | |
| CaMg | 1D | 164,460 | -1.95 | 3.329 | +0.001 | 0.02723 | +0.66 |
| | 2N | 182,930 | -2.06 | 1.812 | -0.006 | 0.02148 | +0.69 |
| | 3D | 139,837 | -2.93 | 0.4812 | +0.007 | 0.01510 | +1.00 |
| | 4N1 | 158,721 | -4.08 | 0.4169 | +0.018 | 0.01380 | +1.40 |
| Ca-rich | 1D | 168,619 | -4.58 | 0.5096 | -0.001 | 0.01446 | +1.57 |
| | 2N | 170,174 | -1.78 | 0.9692 | +0.002 | 0.01786 | +0.60 |
| | 3D | 154,464 | -3.25 | 3.264 | -0.002 | 0.02765 | +1.11 |
| | 4N1 | 164,264 | -4.11 | 0.4416 | +0.013 | 0.01390 | +1.41 |
| Ca-S | 4N2 | 226,767 | -2.51 | 0.7815 | +0.011 | 0.01510 | +0.85 |
| | 1D | 150,539 | -4.13 | 1.536 | +0.002 | 0.02169 | +1.42 |
| | 2N | 173,558 | +2.94 | 0.7619 | -0.007 | 0.01637 | -0.58 |
| | 3D | 163,259 | -4.15 | 0.9654 | +0.004 | 0.01808 | +1.42 |
| | 4N | 161,819 | -2.78 | 0.6821 | -0.001 | 0.01615 | +0.94 |

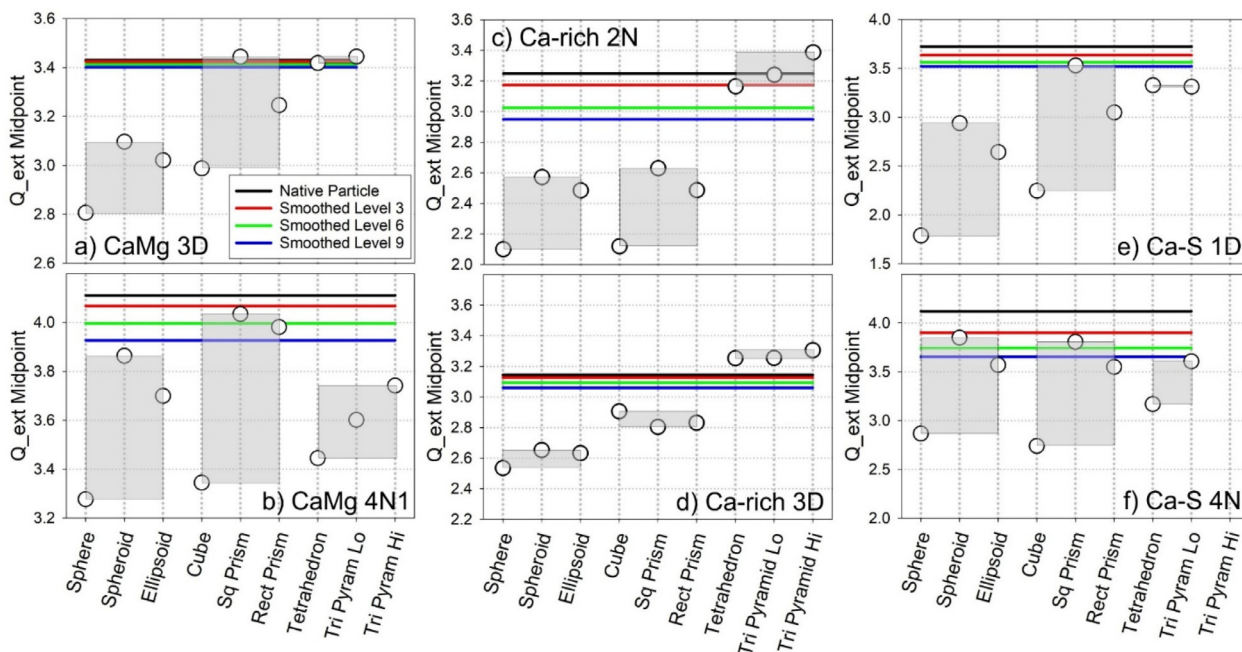


Fig. 15. Midpoints of the extinction efficiency for geometric shapes (circles) and after smoothing of selected particles at levels 3, 6 and 9 (horizontal lines). a) to d) Asian dust; e) and f) background marine air particles. Shaded areas show the extent of variation within each shape group. For comparison, y-axes have the same range between the two examples for the CaMg, Ca-rich, and Ca-S particles.

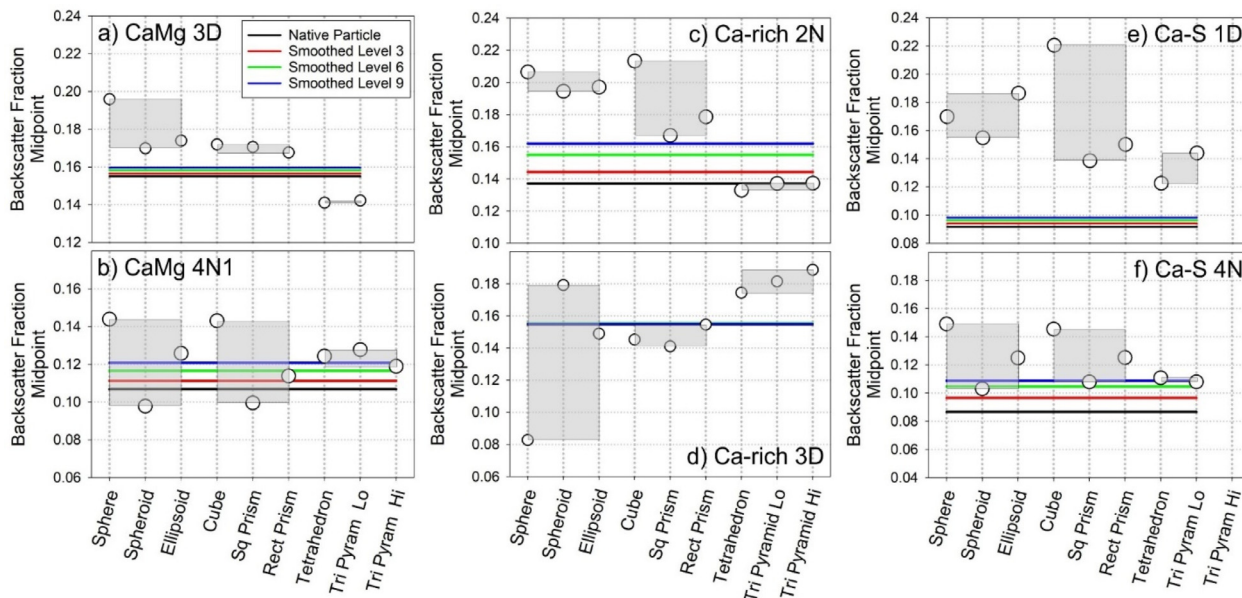


Fig. 16. Midpoints of the backscatter fraction for geometric shapes (circles) and after smoothing of selected particles at levels 3, 6 and 9 (horizontal lines). a) to d) Asian dust; e) and f) background marine air particles. Shaded areas show the extent of variation within each shape group. For comparison, y-axes have the same range between the two examples for the CaMg, Ca-rich, and Ca-S particles.

spheroid as well as square prism has only slightly more surface area than the sphere and cube, respectively (Fig. 14). If surface roughness was a factor, we would expect the sphere and cube to also approximate the particle's extinction.

The Ca-rich particles 2N and 3D in Fig. 15c and d present a different situation. In Fig. 15c, smoothing decreases extinction substantially (10%) and only the tetrahedron and triangular pyramid approximate the particle's extinction efficiency. In this case, the additional surface area of the pyramid shapes allows these shapes to account for the particle's surface roughness. Surface roughness may also be a factor in approximating the extinction efficiency of particle 3D (Fig. 15d) even though surface roughness only accounts

for 3% of the extinction. The shaded areas show much less variation in extinction within each shape group compared to that for the Ca-rich 2N case (Fig. 15c). As mentioned previously, particle 3D absorbed substantially more at 589 nm than other particles in this study. It has been suggested that surface roughness becomes a more important factor for particles with higher absorptivities [33]. It appears in Fig. 15d that the additional surface area of the pyramid shapes caused them to slightly overestimate the extinction efficiency.

In Fig. 16, we look at how the backscatter fraction of the geometric shapes compares with the particles after removing surface roughness. As with extinction, the gradation in the backscat-

ter fraction due to smoothing is shown by the series of horizontal lines in each plot of Fig. 16. The black lines indicate the backscatter fraction without smoothing. For particles CaMg 3D, Ca-rich 3D, and Ca-S 1D in Figs. 16a, d, and e, surface roughness has minimal effect on the backscatter fraction compared to the extent of variation within each shape group. Thus, for these particles geometric shapes do not effectively account for surface roughness.

Figs. 16b and f show that for particles CaMg 4N1 and Ca-S 4N surface roughness is also not likely a factor in how well the shapes approximate the backscatter fraction. The reason is that while the spheroid and square prism come closest to the particle's backscatter fraction, the sphere and cube are far from it. As with extinction, if surface roughness was a factor, we would expect the sphere and cube to also approximate the particles' backscatter fraction due to the similarity in their surface area with the spheroid and square prism, respectively.

As with extinction, particle Ca-rich 2N in Fig. 16c presents a different situation. In this case, surface roughness is likely a factor that allows the pyramid shapes with their additional surface area to approximate the backscatter fraction of particle Ca-rich 2N. It appears that the pyramid shapes approximate both the extinction and backscatter fraction of Ca-rich 2N because these shapes accounted for surface roughness.

5. Conclusion

In this work, we compared the scattering intensity, degree of linear polarization, extinction efficiency, and backscatter fraction of single atmospheric dust particles collected at Mauna Loa Observatory with a series of simple geometric shapes grouped as ellipsoids, cuboids, and pyramids. Within each group, shapes with 1, 2, and 3 differing axes represented a progression such that the 1-axis and 2-axis shapes (lower-order shapes) would be less faithful to the particle's dimensions and the 3-axis shapes (higher-order) would be the more faithful to the particle's dimensions. While the higher-order ellipsoid and rectangular prism were perhaps closer to the particles' dimensions, they were not necessarily better in approximating the extinction efficiency and backscatter fraction than lower-order 2-axis shapes.

Most geometric shapes in this work underestimated the extinction efficiency for the 13 particles studied. 64% to 76% of shapes underestimated the Asian dust particles while 100% of shapes underestimated the background marine air particles. For the Asian dust, $\geq 93\%$ of the ellipsoid group shapes and 67% to 92% of the cuboid shapes underestimated extinction. However, only 29% to 30% of the pyramid shapes underestimated extinction. In general, the pyramid shapes, particularly the tetrahedron, exhibited much less variation in extinction efficiency, relative to variation among the particles, compared to other shapes.

In contrast to extinction, most geometric shapes overestimated the backscatter fraction with 59% to 79% of shapes overestimating the Asian dust and 100% of shapes overestimating the background marine air particles. For the Asian dust, 75% to 80% of the ellipsoid group shapes and 60% to 83% of the cuboid shapes overestimated the backscatter fraction. However, the pyramid shapes overestimated the backscatter fraction to a lesser extent, with 64% of the pyramid shapes underestimating or closely approximating the backscatter fraction for the Ca-rich particles.

In this study, the pyramid shapes, tetrahedron and triangular pyramid, performed best in approximating the extinction efficiency and generally as well as other 2- and 3-axis shapes in approximating the backscatter fraction. In some cases, the success of the pyramid shapes may be attributed to their high angularity and larger surface area which may account for the additional extinction (and the decrease in the backscatter fraction) of the particles

due to surface roughness. Nevertheless, the pyramid shapes, particularly the tetrahedron, exhibited much less variation in extinction efficiency, relative to variation among the particles, compared to other shapes. This aspect may limit the versatility of tetrahedra as a shape model for an ensemble of particles.

Further studies of the optical properties of single atmospheric particles and comparisons with geometric shapes with high angularity should be undertaken. To account for surface roughness, we suggest that shapes such as pyramids with increased surface area, relative to spheroids, be considered in aerosol models for remote sensing. Tetrahedra offer an advantage in that additional parameterization of the aerosol model with shape aspect ratios is not necessary.

Declaration of Competing Interest

The authors declare that they have no known competing financial interests or personal relationships that could have appeared to influence the work reported in this paper.

CRediT authorship contribution statement

Joseph M. Conny: Conceptualization, Methodology, Software, Formal analysis, Investigation, Writing - original draft, Writing - review & editing, Visualization, Supervision. **Robert D. Willis:** Formal analysis, Investigation, Resources, Writing - review & editing. **Diana L. Ortiz-Montalvo:** Validation, Formal analysis, Investigation, Writing - review & editing, Visualization.

Acknowledgments

We thank Aidan Colton of the National Oceanic and Atmospheric Administration, Hilo, Hawaii for assistance in aerosol sampling at MLO. We also thank Cynthia Zeissler of NIST for a thoughtful review of the manuscript.

Supplementary materials

Supplementary material associated with this article can be found, in the online version, at doi:[10.1016/j.jqsrt.2020.107197](https://doi.org/10.1016/j.jqsrt.2020.107197). Additional data can be found at the website <https://doi.org/10.18434/M32263>.

References

- [1] Boucher O, Randall D, Artaxo P, Bretherton C, Feingold G, Forster P, et al. Clouds and Aerosols Climate Change 2013: The Physical Science Basis Contribution of Working Group I to the Fifth Assessment Report of the Intergovernmental Panel on Climate Change. Stocker TF, Qin D, Plattner G-K, Tignor M, Allen SK, Boschung J, et al., editors. Cambridge, U.K. and New York, NY, USA: Cambridge University Press; 2013.
- [2] Claquin T, Schulz M, Balkanski Y, Boucher O. Uncertainties in assessing radiative forcing by mineral dust. *Tellus Series B-Chemical and Physical Meteorology* 1998;50:491–505.
- [3] Prospero JM, Ginoux P, Torres O, Nicholson SE, Gill TE. Environmental characterization of global sources of atmospheric soil dust identified with the Nimbus 7 total ozone mapping spectrometer (TOMS) absorbing aerosol product. *Rev Geophys* 2002;40:2-1-2-31.
- [4] Buseck PR, Posfai M. Airborne minerals and related aerosol particles: effects on climate and the environment. *Proc Natl Acad Sci USA* 1999;96:3372–9.
- [5] Shao YP, Wyrwoll KH, Chappell A, Huang JP, Lin ZH, McTainsh GH, et al. Dust cycle: An emerging core theme in Earth system science. *Aeolian Res* 2011;2:181–204.
- [6] Sokolik IN, Toon OB. Direct radiative forcing by anthropogenic airborne mineral aerosols. *Nature* 1996;381:681–3.
- [7] Tegen I, Lacis AA, Fung I. The influence on climate forcing of mineral aerosols from disturbed soils. *Nature* 1996;380:419–22.
- [8] Conny JM, Norris GA. Scanning electron microanalysis and analytical challenges of mapping elements in urban atmospheric particles. *Env Sci Technol* 2011;45:7380–6.
- [9] Reid EA, Reid JS, Meier MM, Dunlap MR, Cliff SS, Broumas A, et al. Characterization of African dust transported to Puerto Rico by individual particle and size segregated bulk analysis. *J Geophysical Res-Atmos* 2003;108.

- [10] Nousiainen T, Kandler K. Light scattering by atmospheric mineral dust particles. In: Kokhanovsky AA, editor. *Light Scattering Reviews* 2015;9:3–52.
- [11] Kandler K, Lieke K, Benker N, Emmel C, Kupper M, Muller-Ebert D, et al. Electron microscopy of particles collected at Praia, Cape Verde, during the Saharan Mineral Dust Experiment: particle chemistry, shape, mixing state and complex refractive index. *Tellus Series B-Chemical and Physical Meteorology* 2011;63:475–96.
- [12] Jackson JM, Liu H, Laszlo I, Kondragunta S, Remer LA. Suomi-NPP VIIRS aerosol algorithms and data products. *J Geophys Res-Atmos* 2013;118:12673–89.
- [13] Liu H, Remer LA, Huang J, Huang H-C, Kondragunta S. Preliminary evaluation of S-NPP VIIRS aerosol optical thickness. *J Geophys Res-Atmos* 2014;119:3942–62.
- [14] Remer LA, Kaufman YJ, Tanré D, Mattoo S, Chu DA, Martins JV, et al. The MODIS Aerosol Algorithm, Products, and Validation. *J Atmos Sci* 2005;62:947–73.
- [15] Levy RC, Munchak LA, Mattoo S, Patadia F, Remer LA, Holz RE. Towards a long-term global aerosol optical depth record: applying a consistent aerosol retrieval algorithm to MODIS and VIIRS-observed reflectance. *Atmos Meas Tech* 2015;8:4083–110.
- [16] Kahn RA, Gaitley BJ. An analysis of global aerosol type as retrieved by MISR. *J Geophys Res-Atmos* 2015;120:4248–81.
- [17] Kahn RA, Gaitley BJ, Garay MJ, Diner DJ, Eck TF. Multiangle Imaging Spectro-Radiometer global aerosol product assessment by comparison with the Aerosol Robotic Network. *J Geophys Res* 2010;115.
- [18] Holben BN, Eck TF, Slutsker I, Tanré D, Buis JP, Setzer A, et al. AERONET—A Federated Instrument Network and Data Archive for Aerosol Characterization. *Remote Sensing Env* 1998;66:1–16.
- [19] Dubovik O, Holben B, Eck TF, Smirnov A, Kaufman YJ, King MD, et al. Variability of absorption and optical properties of key aerosol types observed in worldwide locations. *J Atmos Sci* 2002;59:590–608.
- [20] Liu ZY, Vaughan M, Winker D, Kittaka C, Getzewich B, Kuehn R, et al. The CALIPSO Lidar Cloud and Aerosol Discrimination: Version 2 Algorithm and Initial Assessment of Performance. *J Atmos Ocean Technol* 2009;26:1198–213.
- [21] Vaughan MA, Powell KA, Kuehn RE, Young SA, Winker DM, Hostetler CA, et al. Fully Automated Detection of Cloud and Aerosol Layers in the CALIPSO Lidar Measurements. *J Atmos Ocean Technol* 2009;26:2034–50.
- [22] Wang MH, Gordon HR. Estimating aerosol optical properties over the oceans with the multiangle imaging spectroradiometer: some preliminary studies. *Appl Opt* 1994;33:4042–57.
- [23] Kahnert M, Nousiainen T, Lindqvist H. Review: Model particles in atmospheric optics. *J Quant Spectrosc Radiat Transf* 2014;146:41–58.
- [24] Hill SC, Hill AC, Barber PW. Light scattering by size/shape distributions of soil particles and spheroids. *Applied Optics* 1984;23:1031.
- [25] Mishchenko MI, Travis LD, Kahn RA, West RA. Modeling phase functions for dustlike tropospheric aerosols using a shape mixture of randomly oriented polydisperse spheroids. *J Geophys Res-Atmos* 1997;102:16831–47.
- [26] Dubovik O, Sinyuk A, Lapyonok T, Holben BN, Mishchenko M, Yang P, et al. Application of spheroid models to account for aerosol particle nonsphericity in remote sensing of desert dust. *J Geophys Res-Atmos* 2006;111:34.
- [27] Nousiainen T, Kahnert M, Veihelmann B. Light scattering modeling of small feldspar aerosol particles using polyhedral prisms and spheroids. *J Quant Spectrosc Radiat Transf* 2006;101:471–87.
- [28] Mishchenko MI, Lacis AA, Carlson BE, Travis LD. Nonsphericity of dust-like tropospheric aerosols: Implications for aerosol remote sensing and climate modeling. *Geophys Res Lett* 1995;22:1077–80.
- [29] Mishchenko MI, Travis LD, Lacis AA. Chapter 10. Scattering and Absorption Properties of Nonspherical Particles. Scattering, Absorption, and Emission of Light by Small Particles. Cambridge, UK: Cambridge University Press; 2002.
- [30] Levy RC, Remer LA, Dubovik O. Global aerosol optical properties and application to Moderate Resolution Imaging Spectroradiometer aerosol retrieval over land. *J Geophys Res-Atmos* 2007;112.
- [31] Mishchenko MI, Travis LD, Macke A. Scattering of light by polydisperse, randomly oriented, finite circular cylinders. *Appl Opt* 1996;35:4927–40.
- [32] Zubko E, Muinonen K, Munoz O, Nousiainen T, Shkuratov Y, Sun WB, et al. Light scattering by feldspar particles: Comparison of model agglomerate debris particles with laboratory samples. *J Quant Spectrosc Radiat Transf* 2013;131:175–87.
- [33] Rother T, Schmidt K, Wauer J, Shcherbakov V, Gayet JF. Light scattering on Chebyshev particles of higher order. *Appl Opt* 2006;45:6030–7.
- [34] Kahnert M, Rother T. Modeling optical properties of particles with small-scale surface roughness: combination of group theory with a perturbation approach. *Opt Express* 2011;19:11138–51.
- [35] Li CH, Kattawar GW, Yang P. Effects of surface roughness on light scattering by small particles. *J Quant Spectrosc Radiat Transf* 2004;89:123–31.
- [36] Zubko E, Muinonen K, Shkuratov Y, Videen G, Nousiainen T. Scattering of light by roughened Gaussian random particles. *J Quant Spectrosc Radiat Transf* 2007;106:604–15.
- [37] Mishchenko MI, Dlugach JM, Mackowski DW. Light scattering by wavelength-sized particles "dusted" with subwavelength-sized grains. *Opt Lett* 2011;36:337–9.
- [38] Kempainen O, Nousiainen T, Lindqvist H. The impact of surface roughness on scattering by realistically shaped wavelength-scale dust particles. *J Quant Spectrosc Radiat Transf* 2015;150:55–67.
- [39] Nousiainen T, Zubko E, Lindqvist H, Kahnert M, Tyynela J. Comparison of scattering by different nonspherical, wavelength-scale particles. *J Quant Spectrosc Radiat Transf* 2012;113:121–35.
- [40] Jeong GY, Nousiainen T. TEM analysis of the internal structures and mineralogy of Asian dust particles and the implications for optical modeling. *Atmospheric Chemistry and Physics* 2014;14:7233–54.
- [41] Kalashnikova OV, Sokolik IN. Modeling the radiative properties of nonspherical soil-derived mineral aerosols. *J Quantitative Spectroscopy Radiat Transf* 2004;87:137–66.
- [42] Merikallio S, Lindqvist H, Nousiainen T, Kahnert M. Modelling light scattering by mineral dust using spheroids: assessment of applicability. *Atmos Chem Phys* 2011;11:5347–63.
- [43] Lindqvist H, Jokinen O, Kandler K, Scheuvs D, Nousiainen T. Single scattering by realistic, inhomogeneous mineral dust particles with stereogrammetric shapes. *Atmos Chem Phys* 2014;14:143–57.
- [44] Conny JM, Willis RD, Ortiz-Montalvo DL. Analysis and Optical Modeling of Individual Heterogeneous Asian Dust Particles Collected at Mauna Loa Observatory. *J Geophys Res-Atmos* 2019;124:2702–23.
- [45] Draine BT, Flatau PJ. Discrete-dipole approximation for scattering calculations. *J Opt Soc Am* 1994;11.
- [46] Nousiainen T, Zubko E, Niemi JV, Kupiainen K, Lehtinen M, Muinonen K, et al. Single-scattering modeling of thin, birefringent mineral-dust flakes using the discrete-dipole approximation. *J Geophys Res-Atmos* 2009;114:12.
- [47] Dabrowska DD, Munoz O, Moreno F, Nousiainen T, Zubko E, Marra AC. Experimental and simulated scattering matrices of small calcite particles at 647 nm. *J Quant Spectrosc Radiat Transf* 2013;124:62–78.
- [48] Sokolik IN, Toon OB. Incorporation of mineralogical composition into models of the radiative properties of mineral aerosol from UV to IR wavelengths. *J Geophysical Res* 1999;104:9423–44.
- [49] Lafon S, Sokolik IN, Rajot JL, Caquineau S, Gaudichet A. Characterization of iron oxides in mineral dust aerosols: Implications for light absorption. *J Geophys Res-Atmos* 2006;111:19.
- [50] Conny JM. The internal composition of atmospheric dust particles from focused ion-beam scanning electron microscopy. *Env Sci Tech* 2013;47:8575–81.
- [51] Conny JM, Collins SM, Herzing AA. Qualitative Multiplatform Microanalysis of Individual Heterogeneous Atmospheric Particles from High-Volume Air Samples. *Analytical Chemistry* 2014;86:9709–16.
- [52] Conny JM, Ortiz-Montalvo DL. Effect of heterogeneity and shape on optical properties of urban dust based on three-dimensional modeling of individual particles. *J Geophys Res-Atmos* 2017;122:9816–42.
- [53] Draine BT, Flatau PJ. User Guide for the Discrete Dipole Approximation Code DDSCAT 7.3. 2013. p. 101.
- [54] Wadell H. Volume, shape, and roundness of quartz particles. *J Geology* 1935;43:250–80.
- [55] Bohren CF, Wickramasinghe NC. On the computation of optical properties of heterogeneous grains. *Astrophysics and Space Science* 1977;50:461–72.
- [56] Bohren CF, Huffman DR. Absorption and Scattering of Light by Small Particles. Weinheim: Wiley-VCH Verlag GmbH & Co. KGaA; 1983.
- [57] Deer WA, Howie RA, Zussman J. An Introduction to Rock-Forming Minerals. London: The Mineralogical Society; 2013. p. 452.
- [58] Nousiainen T. Optical modeling of mineral dust particles: A review. *J Quantitative Spectrosc Radiat Transf* 2009;110:1261–79.
- [59] Hege HCS, M, Stalling D, Zockler M. A Generalized Marching Cubes Algorithm Based On Non-Binary Classification. Berlin: Zuse Institute Berlin; 1997.
- [60] Support TFVT. Technical question – Generate Surface Module In Avizo. Answers to technical questions regarding how smoothing is performed in Avizo software ed. Houston, TX: Thermo Fisher Scientific; 2019.